SAND2019-9694J

The Coupled Adjoint-State Equation in Forward and Inverse Linear Elasticity: Incompressible Plane Stress

D. Thomas Seidl[a]*, Assad A. Oberai[b], Paul E. Barbone[c]

[a] *Department of Optimization and Uncertainty Quantification, Sandia National Laboratories, Albuquerque NM 87123*
[b] *Department of Aerospace and Mechanical Engineering, University of Southern California, Los Angeles CA 90007*
[c] *Department of Mechanical Engineering, Boston University, Boston, MA 02215*

Abstract

A persistent challenge present in inverse or parameter estimation problems with interior data is how to deal with uncertainty in the boundary conditions employed in the forward or state model. In this work we focus on a linear plane stress inverse elasticity problem with measured displacement data where one component of the measured displacement field is known with considerably greater precision than the other. This situation is commonly encountered when the displacement field is measured using ultrasound or optical coherence tomography. We present a novel computational formulation in which no displacement or traction boundary conditions are assumed. The formulation results in coupling the state and adjoint equations, that are typically uncoupled when a well-posed state model is available. Two variants of residual-based stabilization are added. Our approach is applied to a simulated data set and experimental data from an ultrasound phantom.

Keywords: PDE-constrained optimization, adjoint methods, biomechanical imaging, inverse elasticity, data assimilation

2010 MSC:

*Corresponding author
Email address: dtseidl@sandia.gov (D. Thomas Seidl[a])

1. Introduction

Biomechanical Imaging (BMI) refers to the quantitative mapping of mechanical property distributions of biological tissues for applications in disease diagnosis, monitoring, and treatment. Broadly, in BMI heterogeneous mechanical properties fields within a tissue region of interest are inferred from non-invasive measurements of tissue deformation. The partial differential equation (PDE) used to model the motion of the tissue is invariably the momentum equation. Specific problems differ in the imaging system used to measure displacement or velocity (e.g. ultrasound (US), magnetic resonance imaging (MRI), optical coherence tomography (OCT)), the type of tissue deformation (quasi-static, time-harmonic, or transient), and the constitutive model (e.g. linear elastic, hyperelastic, poroelastic, viscoelastic, anisotropic) employed for the tissue's mechanical response [1].

Image processing techniques applied to medical image (e.g. US, MRI, OCT) data acquired during deformation provide full-field measurements of displacement within an internal tissue region of interest. With US and OCT in particular, these techniques provide highly accurate motion estimates in one direction, the axial or beam direction, but provide much noisier estimates for displacement components along other (referred to as lateral and elevational) directions.

In this work we focus on determination of the linear elastic shear modulus where the deformation is an applied compression that has been measured with these type of displacement estimation techniques. The time scale for the deformation is slow (less than one Hz), so the inertial term in the momentum equation is negligible and can be ignored. Thus the equilibrium equation is the PDE of interest.

For multiple reasons, we choose to utilize an isotropic, incompressible linear plane stress model in this paper. We focus on small ($< 2\%$) strains in this paper which justifies the linear assumption. Further, while three-dimensional displacement field estimation is possible, two-dimensional measurements are predominant. Finally, soft tissue is often assumed to be incompressible because

it contains a significant amount of water.

The choice of plane stress versus plane strain is determined by the loading conditions and the geometry of the sample. Generally speaking if the sample is thin in the out of plane direction, or the loading is confined to small extent in this direction, the plane stress assumption is preferred. In other instances, the plane strain assumption may be more appropriate. Here we focus on plane stress.

The iterative approach to solving the BMI problem can be loosely described as a guided guess and check procedure. One begins with an initial shear modulus distribution and numerically computes the displacement field that results from that distribution by solving the equilibrium equation. The displacement field predicted by the model is then quantitatively compared to the measurements. The mechanical property field is varied in a manner that will diminish the mismatch between the measurements and predictions through the use of optimization, and the process repeats until a convergence criterion is met. Formally, this process known as PDE-constrained optimization.

The success of the BMI inversion procedure critically depends on the ability to model the experimental conditions, i.e. the accuracy of the forward model is paramount. In most cases, the deformation in the PDE model is driven solely by displacement boundary conditions (BCs) inferred from the measurements, as we assume body forces are negligible. While the measured displacement field is a potential source of Dirichlet data, in practice a pure Dirichlet problem can produce poor modulus reconstructions due to the considerable uncertainty in non-axial components of the measurement. Further, this approach is not viable in incompressible plane strain and 3D as the prescribed BCs will almost certainly not satisfy the incompressibility constraint.

Therefore a mixture of Neumann and Dirichlet data is often used in the forward (also referred to as the state) model. Unfortunately, there are no measurement techniques capable of accurately and non-invasively measuring traction *within* tissue. One strategy, which we refer to as the "assumed BCs" approach, that has found some practical success is to assume that the traction along the

non-axial components of the boundary (i.e. the lateral direction in 2D) vanishes [2]. This assumption introduces a bias into the modulus reconstruction and is thus a potential source of additional error.

It is reasonable to question whether forward boundary conditions are required to determine the modulus distribution under conditions of incompressible plane stress. Babaniyi, et al. [3] show that a single measured displacement component is sufficient to determine the other displacement component up to four undetermined constants, in a medium that is piecewise homogeneous. On the other hand, it is known that when the full displacement field is known, then the modulus distribution is determined up to a single constant [4, 5, 6]. Indeed, direct approaches to the elastic inverse problem for incompressible plane stress [7, 8] demonstrate that when the full displacement field is given, then the inverse problem for modulus can be computed stably with just a single calibration condition. Taken together, these results suggest that, apart from a calibration condition, the shear modulus distribution ought to be determinate without boundary conditions in either the forward or inverse problem.

Previous studies have attempted to address the errors introduced by assuming BCs in forward and inverse elasticity through various means. In [9] "compliance" BCs were estimated and utilized in linear and nonlinear forward elastic materials with application to phantom data and patient-specific models. A similar approach motivated by Bayesian estimation methods leads to elastically restrained or "spring" boundary conditions [10]. In [11] the authors treat the non-axial traction BCs as unknowns to be determined by PDE-constrained optimization in concert with the shear modulus field. Finally, in [12, 13, 14] BC-free variants of the Modified Error in the Constitutive Equation (MECE) approach were presented. Connections between our formulation and the MECE formulation are identified in section 5.2.

Our goal in this paper is to present a computational method for the inverse elasticity problem that *does not require assuming any displacement or traction BCs*. In our path to deriving this method, we first consider the simpler problem of determining the full-field displacement for a problem where the distribution

of the material parameters is known, and a full-field estimate of the displacement field has been measured. We then determine a close-by displacement field that satisfies the physical constraint of the equations of equilibrium. This problem is one of data assimilation and has its own applications independent of the material parameter estimation problem. In the present context, we consider a deterministic data assimilation problem with PDE constraints, and our focus is on identifying reliable discrete representations of that problem. We find that even in the linear data assimilation context, the discretized PDE constraint cannot be used to estimate the system's state when displacement and traction BCs are absent. Therefore, we introduce two residual-based stabilization schemes to ensure the stability of the discretization. We make the observation that the Euler-Lagrange equations describe a *coupled* system that consists of the normally *uncoupled* state and adjoint PDEs present in the inverse problem formulation, which motivates the name for our method and the title of this paper.

Once an appropriate discrete representation of the system and its update is available, that update can be accomplished by any of a variety of methods including a Kalman filter. The Kalman filter and its variants (e.g. extended, unscented, ensemble) have been successfully applied to a wide range of discrete, stochastic, data assimilation problems [15, 16, 17]. We note, however, that the Kalman filter is often modified when applied to systems with state constraints [18], as is the case here.

After developing a method for determining the full-field displacement we return to the inverse elasticity problem of estimating the material parameters. There we employ this method to determine the adjoint-based computation of the gradient of the inverse problem objective function with respect to the material parameter field.

The rest of the paper is arranged according to the following outline. First, in section 2 we describe a novel BC-free approach to solving a linear elasticity data assimilation problem called the Coupled Adjoint-State Equation (CASE). Then in section 3 we show how CASE can be used to solve elastic parameter

estimation problems (i.e. inverse elasticity problems). Next, we provide results from the application of CASE to data assimilation and parameter estimation problems with simulated and US phantom data.

After discussing the results in section 5, we also discuss nonlinear extensions to CASE, and identify theoretical connections between CASE and previously published MECE approaches. We conclude with section 6.

2. Data Assimilation Problem

In this section we introduce a variational data assimilation problem for the state field that takes a full-field noisy measurement as input and produces a full-field estimate that satisfies a physics-based constraint as its output. The most novel aspect of this formulation is its complete lack of specification of the BCs normally present in boundary value problems.

We consider an incompressible linear elastic isotropic material. The stress is given by $\boldsymbol{\sigma} = -p\boldsymbol{I} + 2\mu\boldsymbol{\epsilon}$, where p is the pressure, μ is the modulus of rigidity or shear modulus, and $\boldsymbol{\epsilon}$ is the linearized strain. For a thin sheet in plane stress, $\sigma_{33} = 0$ which leads to $p = -2\mu(\epsilon_{xx}+\epsilon_{yy})$. Therefore, we may write the in-plane stress as $\boldsymbol{\sigma} = \mu\boldsymbol{A}(\boldsymbol{u})$, where $\boldsymbol{u}$ represents the in-plane displacement field in the sheet, and $\boldsymbol{A}(\boldsymbol{u}) := 2(\nabla\cdot\boldsymbol{u})\boldsymbol{I} + (\nabla\boldsymbol{u} + \nabla\boldsymbol{u}^T)$ is the incompressible plane stress operator.

The boundary Γ is partitioned into disjoint sections $\Gamma_{\boldsymbol{u}}$ and $\Gamma_{\boldsymbol{t}}$ over which known displacement and traction fields $\boldsymbol{g}$ and $\boldsymbol{h}$ are prescribed, respectively. These partitions must satisfy $\Gamma = \overline{\Gamma_{\boldsymbol{u}} \cup \Gamma_{\boldsymbol{t}}}$ in order for the problem to be well-posed. With negligible body forces, the equilibrium equation and boundary conditions for the sheet are the following:

$$\nabla\cdot[\mu\boldsymbol{A}(\boldsymbol{u})] = \boldsymbol{0} \qquad \text{in } \Omega, \tag{1}$$

$$\boldsymbol{u} = \boldsymbol{g} \qquad \text{on } \Gamma_{\boldsymbol{u}}, \tag{2}$$

$$\mu\boldsymbol{A}(\boldsymbol{u})\cdot\boldsymbol{n} = \boldsymbol{h} \qquad \text{on } \Gamma_{\boldsymbol{t}}. \tag{3}$$

Our goal is to derive a data assimilation formulation that satisfies (1) but does not require (2) or (3). We do so by introducing a Lagrangian that contains (1) as a constraint and a weighted least squares data match term. We assume that a full-field and possibly noise-corrupted measured displacement field $\boldsymbol{u}^m$ is given and the shear modulus is known. The symmetric positive-definite weighting operator $\boldsymbol{T}$ is also known, and its entries are chosen to reflect the component-wise precision in $\boldsymbol{u}^m$.

Throughout this paper we will use the notation $(\cdot,\cdot)$ for the L^2 inner product over Ω and $\|\cdot\|$ for the corresponding norm. Angle brackets $\langle\cdot,\cdot\rangle$ indicate a duality pairing over Γ.

The Lagrangian is

$$\mathcal{L}(\boldsymbol{u},\boldsymbol{w}) = \frac{1}{2}\|\boldsymbol{T}(\boldsymbol{u}-\boldsymbol{u}^m)\|^2 - (\boldsymbol{w}, \nabla\cdot[\mu\boldsymbol{A}(\boldsymbol{u})])\,. \tag{4}$$

2.1. Weak Form

We first perform integration by parts on the constraint term. The function spaces for the forward and adjoint variables are identical in this approach, as there are no essential boundary conditions.

$$-(\boldsymbol{w}, \nabla\cdot[\mu\boldsymbol{A}(\boldsymbol{u})]) = (\nabla\boldsymbol{w}, \mu\boldsymbol{A}(\boldsymbol{u})) - \langle\boldsymbol{w}, \mu\boldsymbol{A}(\boldsymbol{u})\cdot\boldsymbol{n}\rangle \tag{5}$$

$$\boldsymbol{u},\boldsymbol{w} \in \mathcal{V} := \{\boldsymbol{v} \mid v_i \in H^1(\Omega)\} \tag{6}$$

The weak forms that serve as the basis for our computational solution are obtained by taking variations $\delta\boldsymbol{u}$ and $\delta\boldsymbol{w} \in \mathcal{V}$ with respect to $\boldsymbol{u}$ and $\boldsymbol{w}$ by means of the Gâteaux derivative $D_{\boldsymbol{v}}F(\boldsymbol{v})\cdot\delta\boldsymbol{v} := \frac{d}{d\varepsilon}\left[F(\boldsymbol{v}+\varepsilon\delta\boldsymbol{v})\right]\big|_{\varepsilon=0}$. For convenience, we introduce $\boldsymbol{D} := \boldsymbol{T}^T\boldsymbol{T}$.

$$\begin{aligned} D_{\boldsymbol{u}}\mathcal{L}\cdot\delta\boldsymbol{u} &= (\delta\boldsymbol{u}, \boldsymbol{D}(\boldsymbol{u}-\boldsymbol{u}^m)) \\ &\quad + (\nabla\boldsymbol{w}, \mu\boldsymbol{A}(\delta\boldsymbol{u})) - \langle\boldsymbol{w}, \mu\boldsymbol{A}(\delta\boldsymbol{u})\cdot\boldsymbol{n}\rangle \overset{set}{=} 0 \;\forall\delta\boldsymbol{u}\in\mathcal{V} \end{aligned} \tag{7}$$

$$D_{\boldsymbol{w}}\mathcal{L}\cdot\delta\boldsymbol{w} = (\nabla\delta\boldsymbol{w}, \mu\boldsymbol{A}(\boldsymbol{u})) - \langle\delta\boldsymbol{w}, \mu\boldsymbol{A}(\boldsymbol{u})\cdot\boldsymbol{n}\rangle \overset{set}{=} 0 \;\forall\delta\boldsymbol{w}\in\mathcal{V} \tag{8}$$

2.2. Euler-Lagrange Equations

We integrate equations (7) and (8) by parts to determine the Euler-Lagrange equations and natural BCs.

$$
\begin{aligned}
&(\delta\boldsymbol{u}, \boldsymbol{D}(\boldsymbol{u}-\boldsymbol{u}^m) - \nabla\cdot[\mu\boldsymbol{A}(\boldsymbol{w})]) && && (9)\\
&+\langle\delta\boldsymbol{u}, \mu\boldsymbol{A}(\boldsymbol{w})\cdot\boldsymbol{n}\rangle - \langle\boldsymbol{w}, \mu\boldsymbol{A}(\delta\boldsymbol{u})\cdot\boldsymbol{n}\rangle && = 0\ \forall\delta\boldsymbol{u}\in\mathcal{V} &\\
&-(\delta\boldsymbol{w}, \nabla\cdot[\mu\boldsymbol{A}(\boldsymbol{u})]) && = 0\ \forall\delta\boldsymbol{w}\in\mathcal{V} & (10)
\end{aligned}
$$

The last term in (9) is not of standard form, and it is not immediately obvious what natural BC it implies. We show in Appendix A that it implies that $\boldsymbol{w}$ vanishes on the boundary. Using this result and equations (9) and(10) we state the Euler-Lagrange equations:

$$
\begin{aligned}
\nabla\cdot[\mu\boldsymbol{A}(\boldsymbol{u})] &= \boldsymbol{0} && \text{in } \Omega, && (11)\\
\boldsymbol{D}\boldsymbol{u} - \nabla\cdot[\mu\boldsymbol{A}(\boldsymbol{w})] &= \boldsymbol{D}\boldsymbol{u}^m && \text{in } \Omega, && (12)\\
\boldsymbol{w} &= \boldsymbol{0} && \text{on } \Gamma, && (13)\\
\mu\boldsymbol{A}(\boldsymbol{w})\cdot\boldsymbol{n} &= \boldsymbol{0} && \text{on } \Gamma. && (14)
\end{aligned}
$$

This system of coupled equations has no BCs specified on the displacement field, however, the Lagrange multiplier has two BCs.

2.3. Discretization

We now discretize the weak forms (7) and (8) and introduce some notation that will be used throughout the article. We discretize $\boldsymbol{u}$ and $\boldsymbol{w}$ with finite element basis functions to obtain the discretized solution fields $\boldsymbol{u}^h := u_i^b N_b(\boldsymbol{x})$ and $\boldsymbol{w}^h := w_i^a N_a(\boldsymbol{x})$. The discrete representations of the shear modulus field μ^h and weighting tensor $\boldsymbol{D}^h$ are expressed in a similar fashion.

$$(\delta \boldsymbol{u}, \boldsymbol{D}\boldsymbol{u}) \xRightarrow{\text{disc.}} \int_\Omega \delta u_i^a N_a D_{ij}^c N_c N_b u_j^b \; d\Omega \longleftrightarrow \{\delta u\}^T [M_D] \{u\} \tag{15}$$

$$(\nabla \delta \boldsymbol{w}, \mu \boldsymbol{A}(\boldsymbol{u})) \xRightarrow{\text{disc.}} \int_\Omega \delta w_i^a N_{a,j} \mu^c N_c A(\boldsymbol{u}^b N_b)_{ij} \; d\Omega \longleftrightarrow \{\delta w\}^T [K] \{u\} \tag{16}$$

$$\langle \delta \boldsymbol{w}, \mu \boldsymbol{A}(\boldsymbol{u}) \cdot \boldsymbol{n} \rangle \xRightarrow{\text{disc.}} \int_\Gamma \delta w_i^a N_a \mu^c N_c A(\boldsymbol{u}^b N_b)_{ij} n_j \; d\Gamma \longleftrightarrow \{\delta w\}^T [B] \{u\} \tag{17}$$

$$(\nabla \boldsymbol{w}, \mu \boldsymbol{A}(\delta \boldsymbol{u})) \xRightarrow{\text{disc.}} \int_\Omega w_i^a N_{a,j} \mu^c N_c A(\delta \boldsymbol{u}^b N_b)_{ij} \; d\Omega \longleftrightarrow \{w\}^T [K] \{\delta u\} \tag{18}$$

$$= \{\delta u\}^T [K]^T \{w\}$$

$$\langle \boldsymbol{w}, \mu \boldsymbol{A}(\delta \boldsymbol{u}) \cdot \boldsymbol{n} \rangle \xRightarrow{\text{disc.}} \int_\Gamma w_i^a N_a \mu^c N_c A(\delta \boldsymbol{u}^b N_b)_{ij} n_j \; d\Gamma \longleftrightarrow \{w\}^T [B] \{\delta u\} \tag{19}$$

$$= \{\delta u\}^T [B]^T \{w\}$$

Putting everything together, we obtain the symmetric block linear system (20). We call this a Coupled Adjoint-State Equation (CASE) system because the adjoint and state PDEs are coupled.

$$\begin{bmatrix} [M_D] & ([K]^T - [B]^T) \\ ([K] - [B]) & \mathbf{0} \end{bmatrix} \begin{Bmatrix} u \\ w \end{Bmatrix} = \begin{Bmatrix} [M_D] u^m \\ \mathbf{0} \end{Bmatrix} \tag{20}$$

The block system (20) violates the discrete inf-sup condition. To see this, we note that both $[M_D]$ and $[K] - [B]$ are $N \times N$. Further, by construction, the rank of $[K] - [B]$ is $m < N$. It must be less than N, for otherwise the state equation, which reads $([K] - [B])u = 0$, would require $u = 0$. Since $([K] - [B])$, is singular, then so is $([K] - [B])^T$. Hence, there are vectors w for which $([K] - [B])^T w = 0$; these directions are not determined by (20). In short, we have too many $w's$. We now present two stabilization approaches that restore solvability to this system by constraining w.

2.4. Stabilization

2.4.1. Weak Stabilization

First we use residual-based stabilization. A Galerkin least-squares term based on equation (13) is appended to the Lagrangian. We scale this term

by a positive constant τ and mesh-dependent parameter h in a manner that is consistent with jump penalization in the discontinuous Galerkin literature [19]. We use $\tau = 1$ for all of the results in the paper, but in practice it may be defined by the user provided it is not $O(\frac{1}{h})$. The stabilized Lagrangian is

$$\mathcal{L}^{\text{STAB}}(\boldsymbol{u}, \boldsymbol{w}) = \mathcal{L}(\boldsymbol{u}, \boldsymbol{w}) - \frac{\tau}{2h} \langle \boldsymbol{w}, \boldsymbol{w} \rangle , \tag{21}$$

and the corresponding weak form is

$$D_{\boldsymbol{w}}\mathcal{L}^{\text{STAB}} \cdot \delta\boldsymbol{w} = D_{\boldsymbol{w}}\mathcal{L} \cdot \delta\boldsymbol{w} - \frac{\tau}{h} \langle \boldsymbol{w}, \delta\boldsymbol{w} \rangle \overset{set}{=} 0 \ \forall \delta\boldsymbol{w} \in \mathcal{V}. \tag{22}$$

We note that the stabilization term is residual-based because as indicated in (13) for the exact solution $\boldsymbol{w} = \boldsymbol{0}$ on Γ and therefore this term vanishes.

In this formulation, a negative semi-definite "mass-like" matrix appears in the lower right block of the saddle point system.

$$\begin{bmatrix} [M_D] & ([K]^T - [B]^T) \\ ([K] - [B]) & -[S] \end{bmatrix} \begin{Bmatrix} u \\ w \end{Bmatrix} = \begin{Bmatrix} [M_D]u^m \\ \boldsymbol{0} \end{Bmatrix} \tag{23}$$

$$\frac{\tau}{h} \int_\Gamma \delta w_i^a \delta_{ij} N_a N_b w_j^b \, d\Gamma \longleftrightarrow \{\delta w\}^T [S] \{w\} \tag{24}$$

2.4.2. Strong Stabilization

Our second approach to stabilizing the discrete saddle point system involves enforcing the natural boundary condition (13) strongly. This is achieved by changing the function space for the Lagrange multiplier $\boldsymbol{w}$ to be

$$\boldsymbol{w} \in \mathcal{V}_0 := \{\boldsymbol{v} \mid v_i \in H^1(\Omega), v_i = 0 \text{ on } \Gamma\}. \tag{25}$$

The corresponding weak forms are

$$D_{\boldsymbol{u}}\mathcal{L} \cdot \delta\boldsymbol{u} = (\delta\boldsymbol{u}, \boldsymbol{D}(\boldsymbol{u} - \boldsymbol{u}^m)) + (\nabla\boldsymbol{w}, \mu\boldsymbol{A}(\delta\boldsymbol{u})) \overset{set}{=} 0 \ \forall \delta\boldsymbol{u} \in \mathcal{V}_0, \tag{26}$$

$$D_{\boldsymbol{w}}\mathcal{L} \cdot \delta\boldsymbol{w} = (\nabla\delta\boldsymbol{w}, \mu\boldsymbol{A}(\boldsymbol{u})) \overset{set}{=} 0 \ \forall \delta\boldsymbol{w} \in \mathcal{V}_0. \tag{27}$$

Note that these equations are simpler than the weak forms in the weakly-stabilized formulation. Upon discretization, we obtain a system similar to (20) where the $[B]$ matrices have disappeared, the $[K]$ matrices are now rectangular, and the overall size of the linear system has been reduced by the number of boundary nodes times two, viz:

$$\begin{bmatrix} [M_D] & [K]^T \\ [K] & \mathbf{0} \end{bmatrix} \begin{Bmatrix} u \\ w \end{Bmatrix} = \begin{Bmatrix} [M_D]u^m \\ \mathbf{0} \end{Bmatrix}. \tag{28}$$

To summarize, in this section we have developed a formulation for determining a physically consistent displacement field from noisy measurements of displacement data. This formulation, which we refer to as CASE, couples the solution of a state problem with that of an adjoint problem. In the next section, we will use CASE to solve an inverse problem for determining the shear modulus.

We would like to note that the forward CASE formulation by itself is also useful. For example, it could find applications in traction force microscopy [20, 21] where the displacement field within a matrix whose material properties are known is measured in response to an unknown traction field that is applied at a boundary. The goal is to determine this traction field. This field could be determined by first recovering the CASE displacement field everywhere in the matrix, and then using this to compute the stress and hence the traction field at the boundary of interest.

3. Inverse Problem Formulation

In this section we introduce an extension of the data assimilation formulation where CASE is used to determine a heterogeneous shear modulus field μ through a PDE-constrained optimization approach. We utilize the following weakly-stabilized Lagrangian as the basis for a BC-free variational formulation of the inverse problem:

$$\mathcal{J}(\boldsymbol{u},\boldsymbol{w},\mu) = \frac{1}{2}\left(\boldsymbol{u}-\boldsymbol{u}^m, \boldsymbol{D}(\boldsymbol{u}-\boldsymbol{u}^m)\right) + \alpha\mathcal{R}(\mu), \tag{29}$$

$$\mathcal{L}^{\mathrm{IP}}(\boldsymbol{u},\boldsymbol{w},\mu) = \mathcal{J} - (\boldsymbol{w}, \nabla\cdot[\mu\boldsymbol{A}(\boldsymbol{u})]) + \frac{\tau}{2h}\left\langle \boldsymbol{w},\boldsymbol{w}\right\rangle, \tag{30}$$

where $\mathcal{J}$ denotes the objective functional and $\mathcal{R}(\mu)$ denotes a regularization operator scaled by a constant α.

The relevant function spaces for $\boldsymbol{u}$ and $\boldsymbol{w}$ are

$$\boldsymbol{u} \in \mathcal{S} := \{\boldsymbol{v} \mid v_i \in H^1(\Omega)\}, \tag{31}$$

$$\boldsymbol{w} \in \mathcal{V} := \{\boldsymbol{v} \mid v_i \in H^1(\Omega)\}, \tag{32}$$

and the function space utilized for μ will depend on the definition of $\mathcal{R}(\mu)$. We note that the strongly-stabilized CASE formulation can be obtained by setting $\mathcal{V} = \mathcal{V}_0 := \{\boldsymbol{v} \mid v_i \in H^1(\Omega), v_i = 0 \text{ on } \Gamma\}$.

Minimization of (30) w.r.t $\boldsymbol{u}$ and $\boldsymbol{w}$ followed by integration by parts yields the weakly-stabilized CASE formulation described in the previous section. We define $\hat{\mathcal{J}}(\mu)$ to be the restriction of (29) to the surface in $(\boldsymbol{u},\boldsymbol{w},\mu)$ space that satisfies the CASE PDEs. We observe that on this surface the strong form equations (11) and (13) imply the equality of $\hat{\mathcal{J}}(\mu)$ and $\mathcal{L}^{\mathrm{IP}}$. Therefore, their variations w.r.t μ will coincide as well, and we can compute the gradient of $\hat{\mathcal{J}}(\mu)$ according to

$$\frac{d\hat{\mathcal{J}}}{d\mu}\cdot\delta\mu = D_\mu\mathcal{L}^{\mathrm{IP}}\cdot\delta\mu = (\nabla\boldsymbol{w}, \delta\mu\boldsymbol{A}(\boldsymbol{u})) - \langle \boldsymbol{w}, \delta\mu\boldsymbol{A}(\boldsymbol{u})\cdot\boldsymbol{n}\rangle + \alpha D_\mu\mathcal{R}\cdot\delta\mu. \tag{33}$$

Thus the iterative solution of the inverse problem proceeds as follows. Given $\boldsymbol{u}^m$ and an initial guess for μ, we solve a CASE data assimilation problem for $\boldsymbol{u}$ and $\boldsymbol{w}$. We can now evaluate the reduced-space objective function $\hat{\mathcal{J}}(\mu)$ and its gradient. These quantities are then passed to a gradient-based optimization algorithm which will return an update to μ. This process repeats until a termination criterion is met and the final μ iterate is taken to be the solution of the inverse problem.

Appendix B contains a more complicated inverse problem formulation where the CASE data assimilation formulation is used to define the PDE constraint in a generic weighted least-squares PDE-constrained optimization problem. All of the inverse results presented in the next section were obtained using the inverse formulation described above in this section.

4. Results

4.1. Simulated Data

We first apply the formulations presented in the previous sections to a simulated dataset motivated by quasi-static US BMI compression experiments with non-dimensionalized units. The 2D shear modulus distribution and applied loading are shown in Figure 1. The shear moduli of the diamond, ellipse, and circle-shaped inclusions are 4, 3, and 2, respectively, and the value of the background is 1. The size of the domain is 70×70, and there are 280 quadrilateral elements along each direction.

The loading is designed to loosely emulate conditions encountered in US elasticity imaging. A constant downward displacement of 0.7 (corresponding to about 1% axial compressive strain) is applied at the top of the domain and the bottom is "stuck", i.e. both components of the displacement field are fixed to zero. The sides of the domain are free to expand. In breast elasticity imaging, the US transducer compresses the tissue, and the chest wall prevents displacement at a greater depth.

Noiseless displacement fields were obtained by solving a forward problem using the loading and reference shear modulus distribution described above as the input to a incompressible linear plane stress finite element model with bilinear shape functions. These displacement fields can then be used as input data to the inverse problem.

Inversion algorithms tend to perform unrealistically well (i.e. commit an "inverse crime") when the same discrete model that was used to generate the data is used to solve the inverse problem. We avoid committing an inverse crime

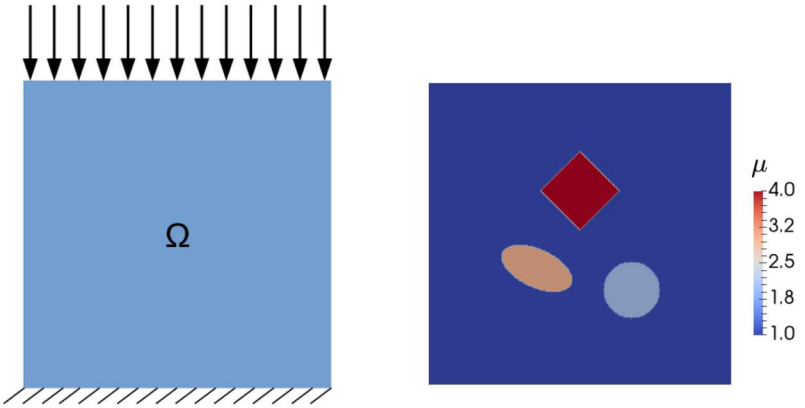

Figure 1: Synthetic inversion problem setup. Left: BCs include a constant downward displacement at the top, no displacement at the bottom, and traction-free sides. Right: The shear modulus distribution contains three inclusions of varying stiffness and shape.

by corrupting the displacements with noise, applying margins to the domain, and downsampling the data.

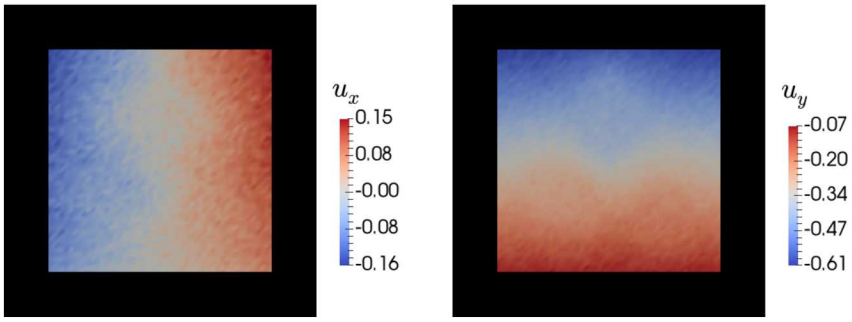

Figure 2: Input data for the inverse problem created by solving a forward problem with the BCs and modulus field shown in Figure 1. The amount of noise added to u_x component is greater than that added to u_y. Margins are applied to the computational domain to emulate experimental conditions encountered in practice.

Additive, independent Gaussian noise $n_i(\boldsymbol{x})$ was added to each displacement component to create simulated "measured" displacement fields $\boldsymbol{u}^m(\boldsymbol{x})$ for the inverse problem. In accordance with US displacement data 2% noise was added to the y component and 10% noise was added to the x component. The formula for % noise is given by equation (35).

Margins of 10 on each side were applied to emulate the fact that in experiments a portion of the interior (rather than the entire physical object) is imaged. Finally, the data were downsampled by a factor of 4 in each direction. After these modifications the dimensions of the computational domain were 50×50 and there were 50 quadrilateral elements along each direction. The synthetic inverse problem data is shown in Figure 2.

$$u_i^m(\boldsymbol{x}) = u_i(\boldsymbol{x}) + n_i(\boldsymbol{x}) \ , \ i = 1, 2 \tag{34}$$

$$\% \text{ noise} = \sqrt{\frac{\int_\Omega n_i^2 \ d\Omega}{\int_\Omega u_i^2 \ d\Omega}} \times 100 \ , \ i = 1, 2 \tag{35}$$

4.1.1. Data Assimilation Results

The CASE formulation can serve as a tool for data assimilation. It takes the measured displacement field $\boldsymbol{u}^m$ and a modulus field μ as input and produces an output predicted displacement field $\boldsymbol{u}$. Our goal in this example is to evaluate errors in CASE as a tool for data assimilation, so for μ we use the exact modulus field evaluated on the 50×50 mesh. The entries of the $\boldsymbol{T}$ weighting tensor (36) present in (4) were chosen to emphasize the axial displacement field over the lateral.

$$[\boldsymbol{T}] = \begin{bmatrix} 0.1 & 0 \\ 0 & 1 \end{bmatrix} \tag{36}$$

Here, T_{xx}/T_{yy} is chosen to be 0.1. Our experience with other values ranging from 0.001 to 0.2, a range of more than two orders of magnitude, resulted in relatively small changes (a few percent) in the recovered shear modulus distributions.

The solutions of the data assimilation problem obtained using weakly-stabilized CASE are shown in Figure 3. They are close to the measurements and satisfy the equilibrium constraint. Figures 4 and 5 display the signed difference between the "exact" (i.e. noiseless downsampled displacement fields with margins applied) and CASE displacement fields δ_x and δ_y. Table 1 reports the L^2 norm

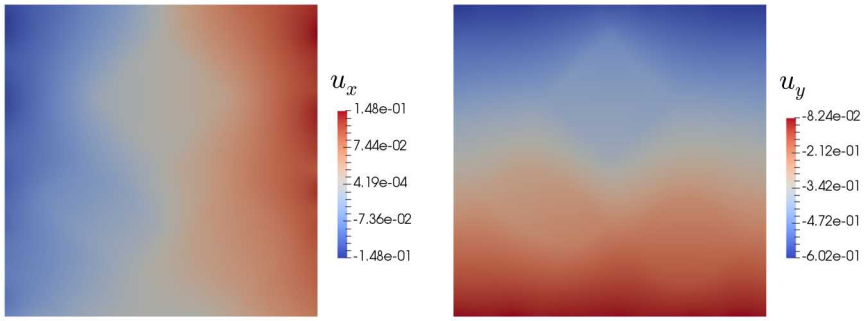

Figure 3: Displacement fields produced by weakly-stabilized CASE driven by the noise-corrupted displacement fields shown in Figure 2. They visually resemble a denoised version of the measurements.

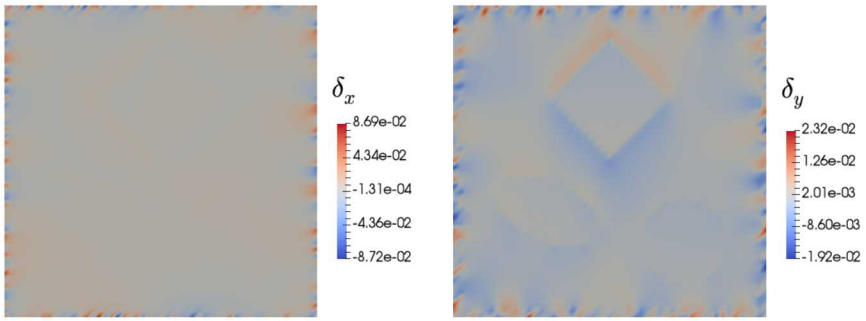

Figure 4: Difference between the "exact" displacement field and CASE output for the strong stabilization formulation. Errors are disproportionately greater near the boundaries.

of the error fields displayed in these figures. In the strong formulation, the errors are largest on the boundary and contain high-frequency noise. The results from the weak formulation display a more even spatial distribution of error, and smoother variation along the boundary. A detailed comparison of the recovered displacement fields by the strong and weak stabilization methods shows them to be nearly identical except for values located within a few element widths of the boundary, where the weak stabilization results are more accurate. Therefore the weak formulation is clearly the more effective of the two with regards to removing noise from measured data. This is supported quantitatively by the values reported in Table 1.

Table 1: L^2 norms of Data Assimilation CASE Solution Errors

Weak δ_x	Weak δ_y	Strong δ_x	Strong δ_y
0.15	0.085	0.38	0.14

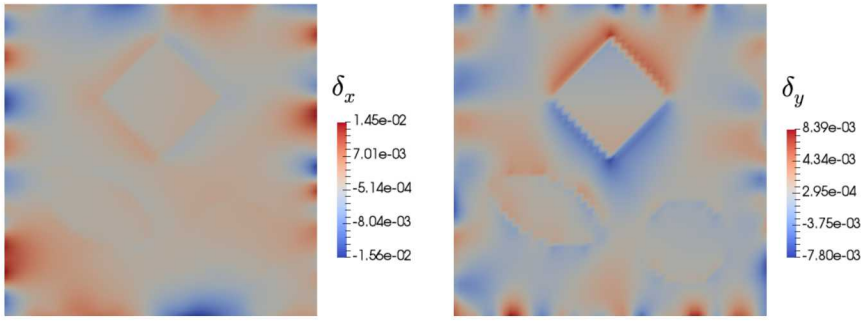

Figure 5: Difference between the "exact" displacement fields and CASE output for the weak stabilization formulation. Error is more evenly dispersed throughout the domain.

4.1.2. Inverse Results

Next we evaluate the use of CASE in the inverse problem. The primary computational tasks in the inversion algorithm are the formation and solution of the block linear system, evaluation of the objective function and its gradient, and calculation of the update to the shear modulus field.

We chose to use $\phi := \log\left(\frac{\mu}{\mu_{\text{ref}}}\right)$ as the optimization variable in the inverse problem rather than μ itself. As discussed in [22], this formulation avoids biasing the solution space by adopting a "stiffness" interpretation (vs compliance) of the material property field. We set $\mu_{\text{ref}} = 1$ in this work.

The gradient-based optimization routine L-BFGS-B [23] was used for minimization. The initial guess for ϕ was 0 (the value of the background), and it was constrained to lie within the interval $[0, \log(10)]$. We terminated the optimization algorithm when the magnitude of the relative reduction in the objective function over five iterations fell below a tolerance, i.e. $|\frac{J^n}{J^{n-5}}| < 10^{-5}$.

We used a total variation (TV) with offset regularization term, as given by equation (37). TV regularization biases the solution space towards piecewise-

constant fields, which is desirable because the true solution is piecewise-constant. We set the regularization constant α to 8×10^{-5}. The offset β regularizes the non-differentiable corner of the absolute value function and was fixed to 1×10^{-3}.

$$\mathcal{R}(\phi) = \int_{\Omega} \sqrt{\nabla\phi \cdot \nabla\phi + \beta^2} \, d\Omega \tag{37}$$

The reconstructed shear modulus fields obtained by both strongly and weakly stabilized formulations are shown in Figure 6. They visually appear to be nearly identical. Thus although the strong and weak stabilization approaches produce notably different displacement fields, the recovered shear modulus fields are quite similar. This finding is significant from a computational implementation and cost standpoint, as the strong approach is considerably easier to implement due to the lack of boundary terms and the size of the block linear system is slightly smaller.

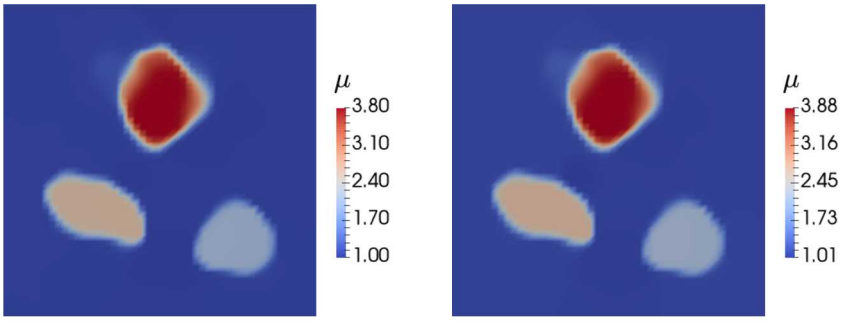

Figure 6: Inverse problem results for the simulated dataset. The weak (left) and strong (right) variants of CASE produce similar modulus fields.

4.2. Experimental Phantom Data

This section contains results from an US phantom study. 2D displacement fields were estimated from radiofrequency US images and analyzed with the CASE-based inverse formulation described in section 3. This data was acquired by Timothy Hall's medical imaging laboratory at the University of Wisconsin,

Madison. Like in the simulated results, we compare the modulus fields reconstructed using the strongly and weakly-stabilized CASE formulations.

The US phantom was a 100 mm cube made of tissue-mimicking agar-gelatin that contained four coplanar 10 mm diameter spherical inclusions, which we refer to as "targets". The procedures used to create, characterize the mechanical properties, and measure the displacement due to compression of the phantom are documented in [24] and [25].

The phantom was imaged with US while being compressed uniformly. A modified block matching method [26] was used to determine the incremental displacement field. Displacement data acquired at roughly 1.5% overall applied strain was used in the CASE inverse problem formulation to estimate the shear modulus distribution.

Figure 7 contains both the measured displacement fields (the input to the inverse problem) and the predicted displacement fields obtained from the weakly-stabilized CASE approach (one of the outputs) for Target 1 (for brevity, the rest of these fields are given in Appendix B). We again observe fluctuations on the boundaries, although unlike in the simulated results they are considerably more pronounced in the lateral displacement field.

The dimensions of the computational domain were 38.8 mm (axial) by 25.8 mm (lateral). The discretization was chosen so that each node in the finite element mesh contained a displacement measurement (i.e. we did not down-sample the measured displacement data), which resulted in a mesh with 53,212 uniformly-sized quadrilateral elements. There were 251 and 212 elements along the axial and lateral directions, respectively, and we employed bilinear finite element shape functions. Thus, the dimension of the parameter space was 53,676.

We now specify details specific to the inverse problem. The entries of the $\boldsymbol{T}$ weighting tensor are the same as those utilized in the simulated dataset and are given by equation (36). A different regularization constant α was utilized in each of the four problems, as the signal-to-noise ratio in each measurement was distinct due to the different moduli of each target. These regularization constants, as well as the contrast between the shear modulus of each inclusion

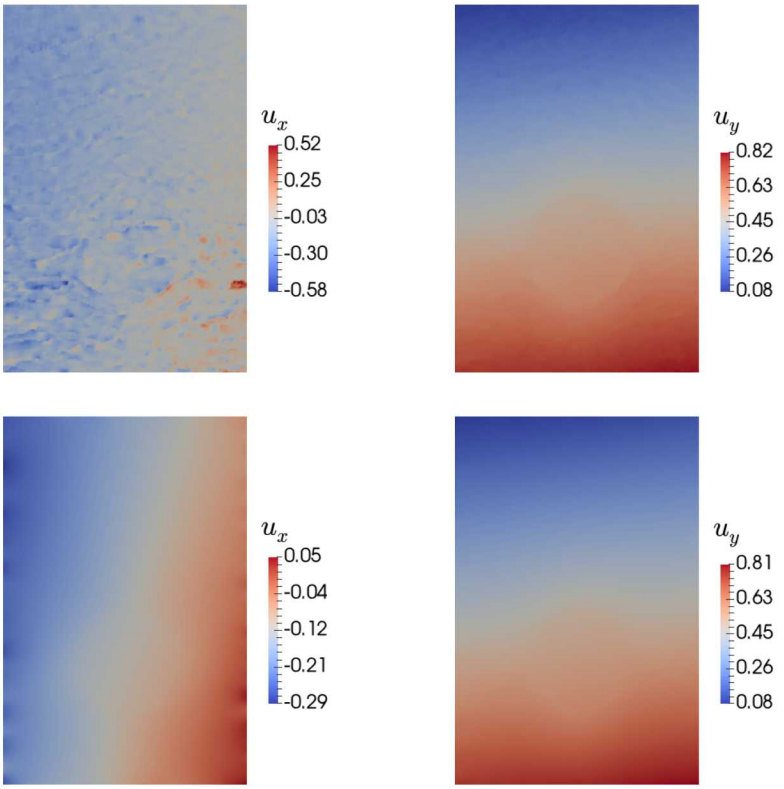

Figure 7: The measured (top row) and predicted (bottom row) displacement fields (in mm) obtained from the weakly-stabilized formulation for Target 1. The amount of noise in the measured lateral displacement field is considerably greater than that observed in the axial field. The lateral displacement field fluctuates on the boundary.

and its background material as measured by independent mechanical testing, are reported in Table 2. The rest of the details that pertain to the optimization, namely optimization algorithm, initial guess, optimization variable transformation, and convergence criterion, are identical to those utilized for the simulated data set.

The reconstructed shear modulus fields for all targets as obtained from the weakly-stabilized CASE formulation are shown in Figure 8. In all cases we observe a roughly circular inclusion embedded within a softer background, and the degree of uniformity of the background and inclusion vary between reconstruc-

Table 2: Regularization constants and reference shear modulus contrasts for the phantom data.

Target	1	2	3	4
α	5.0e-5	6.0e-5	4.0e-5	9.0e-6
Reference Contrast	2.83	2.27	3.54	5.26

tions. The inclusions appear to be slightly elongated along the axial direction, which could be a consequence of the plane stress approximation. We note that the contrasts between the minimum and maximum values of the modulus fields are within 20% and generally lower than the values reported in Table 2.

In Figure 9 we present the signed difference in the shear modulus between the weakly and strongly-stabilized reconstructions. We find that these differences are relatively small compared to the lower bound of the reconstructions. Interestingly, these differences are not confined to the boundaries of the domain, although the largest values (except for Target 3) occur near them. These results, along with those from the simulated data set, suggest that choosing the simpler strongly-stabilized formulation over the weakly-stabilized approach would be beneficial in practice.

5. Discussion

In this section we provide some commentary on our the simulated and experimental results and their broader implications for inverse problems outside of the plane stress model studied in this work. We also include a comparison to the MECE method, another inverse method that avoids prescribing displacement and traction BCs. More specifically, we show that under certain assumptions it closely approximates strongly-stabilized CASE.

First, we find the successful applications of CASE documented in section 4 to be encouraging enough to motivate its extension to other modeling contexts, in particular incompressible plane strain and 3D linear elasticity. A key complication that arises in those models is the need for additional stabilization terms

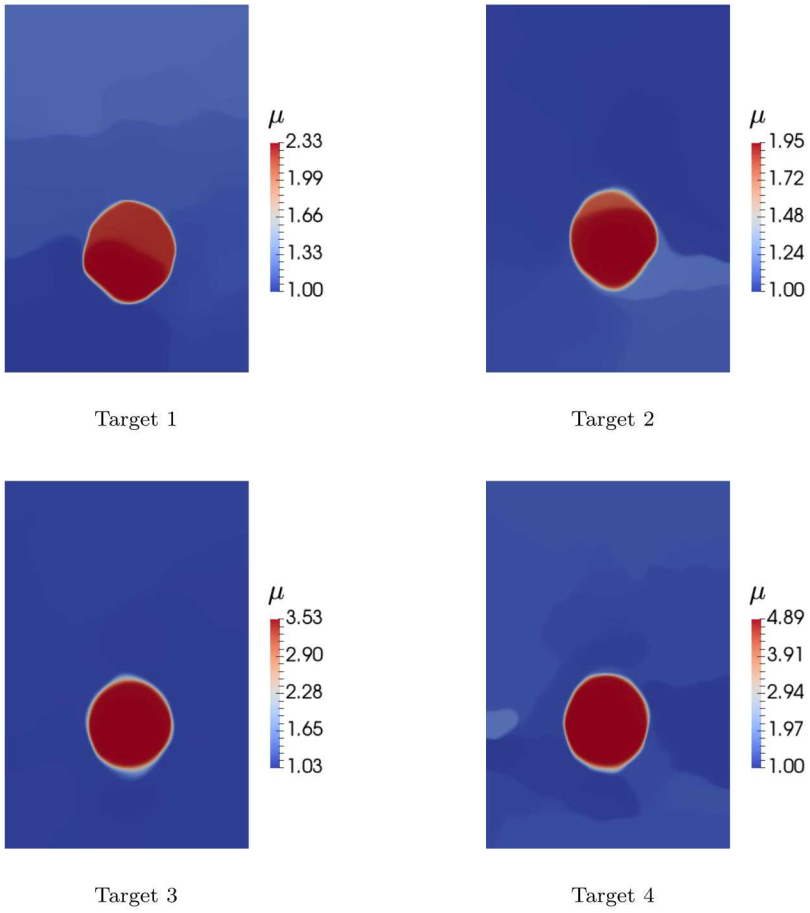

Figure 8: Inversion results from the weakly-stabilized CASE formulation.

due to the presence of the incompressibility constraint. An initial extension to finite-deformation nonlinear elasticity problems is presented in section 5.1.

More generally, we believe that the CASE approach will be useful in any inverse problem that contains a non-negligible amount of uncertainty in the BCs of the PDE constraint. Generalizing CASE to time-harmonic PDEs will be considerably easier than transient PDEs, as in the latter the entire time-histories of the forward and adjoint solutions will be coupled. Several of these extensions have already been considered for the similar MECE approaches discussed in 5.2.

One drawback of CASE, however, is that the cost of solving the coupled

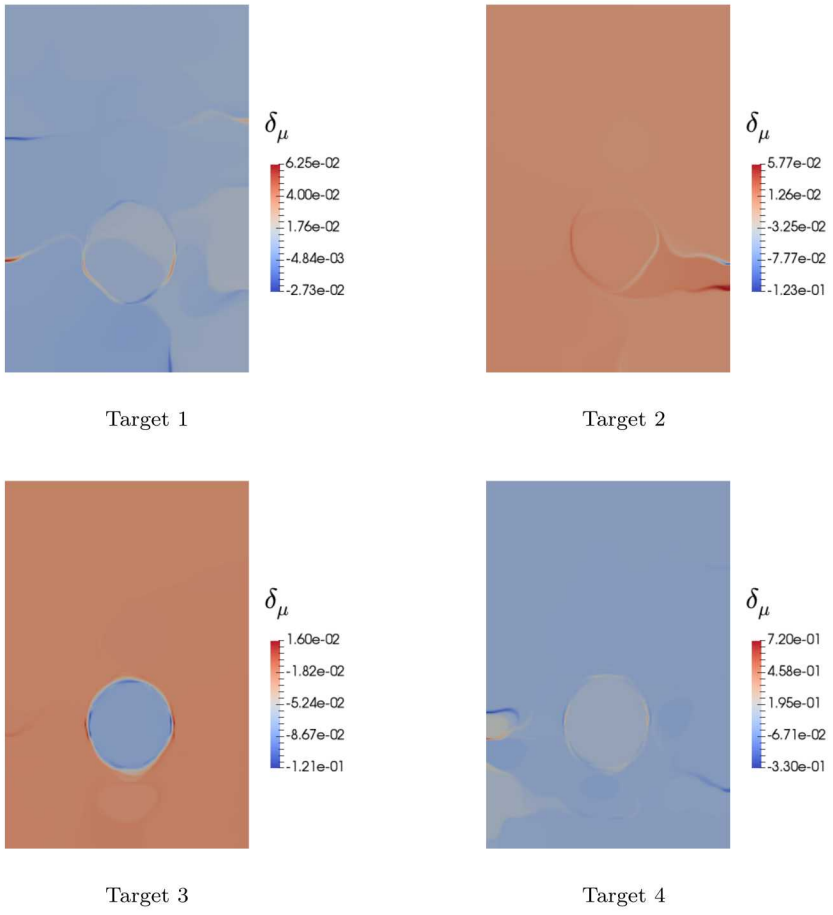

Figure 9: Signed difference between the modulus reconstructions obtained by the strongly and weakly-stabilized approaches.

system at each iteration is increased over that of the decoupled system. We have not observed a noticeable difference in convergence behavior between the coupled and decoupled formulations.

5.1. Nonlinear CASE

We now wish to discuss how CASE changes when the constraint PDE is a nonlinear function of $\boldsymbol{u}$, as would occur in finite-deformation elasticity. In this derivation we only consider the strongly stabilized variant and assume that there exists a generic vector parameter field $\boldsymbol{p}$ that depends on the constitutive

model employed in the constraint. We use the following Lagrangian

$$\mathcal{L}^{\mathrm{NL}}(\boldsymbol{u},\boldsymbol{w}) = \frac{1}{2}\|\boldsymbol{T}(\boldsymbol{u}-\boldsymbol{u}^m)\|^2 - (\boldsymbol{w}, \nabla\cdot\boldsymbol{F}(\boldsymbol{u})\boldsymbol{S}(\boldsymbol{u},\boldsymbol{p}))\,, \tag{38}$$

where $\boldsymbol{F}$ is the deformation gradient and $\boldsymbol{S}$ denotes the second Piola-Kirchhoff stress tensor. We make use of the functions spaces $\mathcal{V}$ and $\mathcal{V}_0$ defined in (6) and (25).

We integrate (38) by parts and use the definition of $\mathcal{V}_0$ to eliminate the boundary terms to obtain

$$\mathcal{L}^{\mathrm{NL}}(\boldsymbol{u},\boldsymbol{w}) = \frac{1}{2}\|\boldsymbol{T}(\boldsymbol{u}-\boldsymbol{u}^m)\|^2 + \mathcal{A}(\boldsymbol{w},\boldsymbol{u};\boldsymbol{p}), \tag{39}$$

where the semilinear form $\mathcal{A}(\boldsymbol{w},\boldsymbol{u};\boldsymbol{p}) := (\nabla\boldsymbol{w}, \boldsymbol{F}\boldsymbol{S})$.

Next we differentiate (39) with respect to each of its arguments to obtain the following weak forms:

$$D_{\boldsymbol{u}}\mathcal{L}^{\mathrm{NL}}\cdot\delta\boldsymbol{u} = (\delta\boldsymbol{u}, \boldsymbol{D}(\boldsymbol{u}-\boldsymbol{u}^m)) + D_{\boldsymbol{u}}\mathcal{A}(\boldsymbol{w},\boldsymbol{u};\boldsymbol{p})\cdot\delta\boldsymbol{u} \overset{set}{=} 0\ \forall\delta\boldsymbol{u}\in\mathcal{V}, \tag{40}$$

$$D_{\boldsymbol{w}}\mathcal{L}^{\mathrm{NL}}\cdot\delta\boldsymbol{w} = \mathcal{A}(\delta\boldsymbol{w},\boldsymbol{u};\boldsymbol{p}) \overset{set}{=} 0\ \forall\delta\boldsymbol{w}\in\mathcal{V}_0. \tag{41}$$

The system represented by (40) and (41) contains a coupled linear PDE (the adjoint equation) and nonlinear PDE (the state equation). We utilize Newton's method to linearize it and solve for the incremental updates $\Delta\boldsymbol{u}$ and $\Delta\boldsymbol{w}$ defined such that $\Delta\boldsymbol{v} := \boldsymbol{v}_{n+1} - \boldsymbol{v}_n$. The coupled linearized system is

$$\begin{aligned}&(\delta\boldsymbol{u}, \boldsymbol{D}\Delta\boldsymbol{u}) + \left\{D_{\boldsymbol{u}}\left[D_{\boldsymbol{u}}\mathcal{A}(\boldsymbol{w}_n,\boldsymbol{u};\boldsymbol{p})\cdot\delta\boldsymbol{u}\right]\cdot\Delta\boldsymbol{u}\right\}\big|_{\boldsymbol{u}=\boldsymbol{u}_n} \qquad (42)\\ &+ \left[D_{\boldsymbol{u}}\mathcal{A}(\Delta\boldsymbol{w},\boldsymbol{u};\boldsymbol{p})\cdot\delta\boldsymbol{u}\right]\big|_{\boldsymbol{u}=\boldsymbol{u}_n} = -\left[D_{\boldsymbol{u}}\mathcal{L}^{\mathrm{NL}}\cdot\delta\boldsymbol{u}\right]\big|_{\boldsymbol{u}=\boldsymbol{u}_n,\boldsymbol{w}=\boldsymbol{w}_n}\ \forall\delta\boldsymbol{u}\in\mathcal{V},\\ &\left[D_{\boldsymbol{u}}\mathcal{A}(\delta\boldsymbol{w},\boldsymbol{u};\boldsymbol{p})\right]\big|_{\boldsymbol{u}=\boldsymbol{u}_n}\cdot\Delta\boldsymbol{u} = -\left[D_{\boldsymbol{w}}\mathcal{L}^{\mathrm{NL}}\cdot\delta\boldsymbol{w}\right]\big|_{\boldsymbol{u}=\boldsymbol{u}_n}\ \forall\delta\boldsymbol{w}\in\mathcal{V}_0. \qquad (43)\end{aligned}$$

We observe that nonlinear CASE contains an extra term that involves two derivatives of the semilinear form. The discrete block linear Newton system is

$$\begin{bmatrix}[M_D]+[N] & [K]^T\\ [K] & \mathbf{0}\end{bmatrix}\begin{Bmatrix}\Delta u\\ \Delta w\end{Bmatrix} = \begin{Bmatrix}-R_u\\ -R_w\end{Bmatrix}, \tag{44}$$

where $[N]$ denotes the discretized term that is exclusive to nonlinear CASE, $[K]$ is now a tangent stiffness matrix, and the vectors R_u and R_w represent the discrete versions of the right hand sides of (42) and (43), respectively. Once u and w are known, we can evaluate the appropriately discretized form of the gradient $D_{\boldsymbol{p}}\mathcal{A}(\boldsymbol{w}, \boldsymbol{u}; \boldsymbol{p}) \cdot \delta\boldsymbol{p}$.

5.2. Comparison to MECE

We would like to compare and contrast CASE to another BC-free elastic inversion technique known as the Modified Error in the Constitutive Equation (MECE) approach. It has been applied to inverse elasticity problems in various contexts such as time-harmonic viscous [12] and non-viscous models [27, 13, 14], fluid-structure interaction [28], and elastodynamics [29].

In the MECE formulation the Cauchy stress $\boldsymbol{\sigma}$ is introduced as an independent variable. In this section we still step away from the plane stress context in which we have been operating to general quasi-static isotropic elasticity where $\boldsymbol{C}$ is a fourth-order tensor with major and minor symmetries that depends linearly on one (incompressible) or two (compressible) elastic constants, which we will collect into the parameter vector $\boldsymbol{p}$. The incompressible plane stress specialization of (45) is recovered by choosing $\boldsymbol{C}$ so that $\boldsymbol{\sigma} = \mu\boldsymbol{A}(\boldsymbol{u})$. In this setting the constitutive equation and strain-displacement relation are

$$\boldsymbol{\sigma} = \boldsymbol{C}\boldsymbol{\epsilon}(\boldsymbol{u}), \tag{45}$$

$$\boldsymbol{\epsilon}(\boldsymbol{u}) = \frac{1}{2}\left(\nabla\boldsymbol{u} + \nabla\boldsymbol{u}^T\right). \tag{46}$$

We assume that body forces are negligible and there are no specified displacement or traction BCs. The MECE Lagrangian is

$$\begin{aligned}\mathcal{L}^{\mathrm{MECE}}(\boldsymbol{\sigma}, \boldsymbol{u}, \boldsymbol{w}, \boldsymbol{p}) &= \frac{1}{2}\|\boldsymbol{T}(\boldsymbol{u} - \boldsymbol{u}^m)\|^2 \\ &+ \frac{1}{2\kappa}\left(\boldsymbol{\sigma} - \boldsymbol{C}\boldsymbol{\epsilon}(\boldsymbol{u}), \boldsymbol{C}^{-1}\left(\boldsymbol{\sigma} - \boldsymbol{C}\boldsymbol{\epsilon}(\boldsymbol{u})\right)\right) + (\nabla\boldsymbol{w}, \boldsymbol{\sigma}) - \langle\boldsymbol{w}, \boldsymbol{\sigma}\cdot\boldsymbol{n}\rangle.\end{aligned} \tag{47}$$

The second term in (47) is a weighted least-squares penalty on the constitutive equation. The constraint term can be simplified by replacing $\nabla \boldsymbol{w}$ with $\boldsymbol{\epsilon}(\boldsymbol{w})$, as $\boldsymbol{\sigma}$ is a symmetric tensor. The constant κ controls the relative importance of matching the data and satisfying the constitutive relation. We require that $0 < \kappa < \infty$. Note that imposing the condition $\boldsymbol{\sigma} = \boldsymbol{C}\boldsymbol{\epsilon}(\boldsymbol{u})$ causes this Lagrangian to be identical to the one we started with for the CASE derivation.

We now make the Lagrangian stationary w.r.t. $\boldsymbol{\sigma}$, $\boldsymbol{u}$, and $\boldsymbol{w}$ and derive the gradient equation for $\boldsymbol{p}$. The relevant function spaces are

$$\mathcal{Z} := \{\boldsymbol{\tau} |\ \tau_{ij} \in L^2(\Omega), \tau_{ij} = \tau_{ji}\}, \tag{48}$$

$$\mathcal{V} := \{\boldsymbol{v} \mid v_i \in H^1(\Omega)\}, \tag{49}$$

$$\mathcal{M} := \{\boldsymbol{m} \mid m_i \in L^\infty(\Omega)\}. \tag{50}$$

The stationary conditions are

$$\begin{aligned} D_{\boldsymbol{\sigma}}\mathcal{L}^{\text{MECE}} \cdot \delta\boldsymbol{\sigma} &= (\frac{1}{\kappa}(\boldsymbol{C}^{-1}\boldsymbol{\sigma} - \boldsymbol{\epsilon}(\boldsymbol{u})) + \boldsymbol{\epsilon}(\boldsymbol{w}), \delta\boldsymbol{\sigma}) - \langle \boldsymbol{w}, \delta\boldsymbol{\sigma} \cdot \boldsymbol{n}\rangle \\ &\overset{set}{=} 0\ \forall \delta\boldsymbol{\sigma} \in \mathcal{Z}, \end{aligned} \tag{51}$$

$$\begin{aligned} D_{\boldsymbol{u}}\mathcal{L}^{\text{MECE}} \cdot \delta\boldsymbol{u} &= (\boldsymbol{D}(\boldsymbol{u} - \boldsymbol{u}^m), \delta\boldsymbol{u}) - \frac{1}{\kappa}\left(\boldsymbol{\sigma} - \boldsymbol{C}\boldsymbol{\epsilon}(\boldsymbol{u}), \boldsymbol{\epsilon}(\delta\boldsymbol{u})\right) \\ &\overset{set}{=} 0\ \forall \delta\boldsymbol{u} \in \mathcal{V}, \end{aligned} \tag{52}$$

$$D_{\boldsymbol{w}}\mathcal{L}^{\text{MECE}} \cdot \delta\boldsymbol{w} = (\boldsymbol{\epsilon}(\delta\boldsymbol{w}), \boldsymbol{\sigma}) - \langle \delta\boldsymbol{w}, \boldsymbol{\sigma} \cdot \boldsymbol{n}\rangle \overset{set}{=} 0\ \forall \delta\boldsymbol{w} \in \mathcal{V}, \tag{53}$$

and the gradient equation is

$$\begin{aligned} D_{\boldsymbol{p}}\mathcal{L}^{\text{MECE}} \cdot \delta\boldsymbol{p} = \frac{\delta\boldsymbol{p}}{\kappa} \cdot \Big[&\frac{1}{2}(\boldsymbol{\sigma} - \boldsymbol{C}\epsilon(\boldsymbol{u}), \frac{d\boldsymbol{C}^{-1}}{d\boldsymbol{p}}(\boldsymbol{\sigma} - \boldsymbol{C}\boldsymbol{\epsilon}(\boldsymbol{u}))) \\ &- (\boldsymbol{\sigma} - \boldsymbol{C}\boldsymbol{\epsilon}(\boldsymbol{u}), \boldsymbol{C}^{-1}\frac{d\boldsymbol{C}}{d\boldsymbol{p}}\boldsymbol{\epsilon}(\boldsymbol{u}))\Big]. \end{aligned} \tag{54}$$

Following [12, 13, 14], we impose the conditions implied by (51) strongly to obtain

$$\boldsymbol{\sigma} = \boldsymbol{C}\boldsymbol{\epsilon}(\boldsymbol{u} - \kappa\boldsymbol{w}) \qquad \text{in } \Omega, \tag{55}$$

$$\boldsymbol{w} = \boldsymbol{0} \qquad \text{on } \Gamma. \tag{56}$$

We observe that the justification for imposing Dirichlet boundary conditions on $\boldsymbol{w}$ strongly originates from (51), while in CASE it comes from (13) which is obtained by taking variations w.r.t. $\boldsymbol{w}$. We introduce $\mathcal{V}_0 \subset \mathcal{V}$ to be

$$\mathcal{V}_0 := \{\boldsymbol{v} \mid v_i \in H^1(\Omega), v_i\big|_\Gamma = 0\}. \tag{57}$$

The weak forms and gradient equation (52)-(54) simplify to

$$\begin{aligned} D_{\boldsymbol{u}}\mathcal{L}^{\text{MECE}} \cdot \delta\boldsymbol{u} &= (\boldsymbol{D}(\boldsymbol{u}-\boldsymbol{u}^m), \delta\boldsymbol{u}) + (\boldsymbol{C}\boldsymbol{\epsilon}(\boldsymbol{w}), \boldsymbol{\epsilon}(\delta\boldsymbol{u})) \\ &\overset{set}{=} 0 \ \forall \delta\boldsymbol{u} \in \mathcal{V}, \end{aligned} \tag{58}$$

$$D_{\boldsymbol{w}}\mathcal{L}^{\text{MECE}} \cdot \delta\boldsymbol{w} = (\boldsymbol{\epsilon}(\delta\boldsymbol{w}), \boldsymbol{C}\boldsymbol{\epsilon}(\boldsymbol{u}-\kappa\boldsymbol{w})) \overset{set}{=} 0 \ \forall \delta\boldsymbol{w} \in \mathcal{V}_0, \tag{59}$$

$$\begin{aligned} D_{\boldsymbol{p}}\mathcal{L}^{\text{MECE}} \cdot \delta\boldsymbol{p} = \delta\boldsymbol{p} \cdot \Big[&\frac{\kappa}{2}(\boldsymbol{C}\epsilon(\boldsymbol{w}), \frac{d\boldsymbol{C}^{-1}}{d\boldsymbol{p}}\boldsymbol{C}\boldsymbol{\epsilon}(\boldsymbol{w})) \\ &+ (\boldsymbol{\epsilon}(\boldsymbol{w}), \frac{d\boldsymbol{C}}{d\boldsymbol{p}}\boldsymbol{\epsilon}(\boldsymbol{u}))\Big]. \end{aligned} \tag{60}$$

We obtain the strong form of the coupled system for $\boldsymbol{u}$ and $\boldsymbol{w}$ by integrating (58) and (59) by parts:

$$\nabla \cdot [\boldsymbol{C}\boldsymbol{\epsilon}(\boldsymbol{w})] = \boldsymbol{D}(\boldsymbol{u}-\boldsymbol{u}^m) \qquad \text{in } \Omega, \tag{61}$$

$$\nabla \cdot [\boldsymbol{C}\boldsymbol{\epsilon}(\boldsymbol{u})] = \kappa\nabla \cdot [\boldsymbol{C}\boldsymbol{\epsilon}(\boldsymbol{w})] \qquad \text{in } \Omega, \tag{62}$$

$$\boldsymbol{w} = \boldsymbol{0} \qquad \text{on } \Gamma, \tag{63}$$

$$\boldsymbol{C}\boldsymbol{\epsilon}(\boldsymbol{w}) \cdot \boldsymbol{n} = \boldsymbol{0} \qquad \text{on } \Gamma. \tag{64}$$

Equations (61) and (62) can be combined to produce

$$\nabla \cdot [\boldsymbol{C}\boldsymbol{\epsilon}(\boldsymbol{u})] = \kappa\boldsymbol{D}(\boldsymbol{u}-\boldsymbol{u}^m) \quad \text{in } \Omega, \tag{65}$$

which implies that a forced version of the equilibrium constraint (1) is satisfied. We note that in the time-harmonic version of MECE the presence of the inertial term makes this reduction to a single PDE for $\boldsymbol{u}$ impossible. A similar manipulation in that context yields

$$\nabla \cdot [\boldsymbol{C}\boldsymbol{\epsilon}(\boldsymbol{u})] + \omega^2 \rho \boldsymbol{u} = \kappa \left[\boldsymbol{D}(\boldsymbol{u} - \boldsymbol{u}^m) - \omega^2 \rho \boldsymbol{w}\right] \quad \text{in } \Omega, \tag{66}$$

where ρ is the density field and ω is the angular frequency of the excitation.

The quasi-static MECE discretized block linear system for the u and w degrees of freedom (borrowing notation from earlier in the paper) is

$$\begin{bmatrix} [M_D] & [K]^T \\ [K] & -\kappa[E] \end{bmatrix} \begin{Bmatrix} u \\ w \end{Bmatrix} = \begin{Bmatrix} [M_D]u^m \\ \mathbf{0} \end{Bmatrix}. \tag{67}$$

The sole difference between the block MECE system (67) and (unregularized) strongly-stabilized CASE (28) is the presence of the $-\kappa[E]$ term in the lower-right block, where $[E]$ is a square matrix that arises from the last term in (59).

MECE resembles CASE most closely when $\kappa \approx 0$. In this scenario for incompressible plane stress we have

$$\boldsymbol{\sigma} \approx \mu \boldsymbol{A}(\boldsymbol{u}), \tag{68}$$

$$\nabla \cdot [\mu \boldsymbol{A}(\boldsymbol{u})] \approx \mathbf{0}, \tag{69}$$

$$D_\mu \mathcal{L}^{\text{MECE}} \cdot \delta\mu \approx (\nabla \boldsymbol{w}, \delta\mu \boldsymbol{A}(\boldsymbol{u})). \tag{70}$$

To summarize, the MECE formulation provides another BC-free approach to solve for $\boldsymbol{u}$ given $\boldsymbol{u}^m$ and $\boldsymbol{p}$. The significant distinctions between it and CASE are the presence of the constant κ, a forced version of the equilibrium equation (65) is satisfied, and the existence of an extra term in the gradient equation (60).

6. Conclusion

In this work we derived the CASE data assimilation formulation and applied it to simulated and experimental datasets associated with the BMI problem. By design, the use of CASE in forward and inverse elasticity problems produces

displacement fields that satisfy the equilibrium PDE without assuming displacement or traction BCs. Of the modulus reconstructions presented in this work, all were within acceptable accuracy ranges defined by either the exact solution in the simulated examples or the experimentally-measured contrast values for the phantom datasets. In particular, compared to reconstructions published previously that were obtained by using measured displacement fields on the boundary [11], the reconstructions obtained by CASE had more accurate contrast and more homogeneous background values. Outside of the linear elastic, incompressible plane stress problems studied in this work, a lack of information with respect to BCs is not uncommon, and we therefore expect modifications and extensions of CASE to be useful in such problems.

Acknowledgements and Funding

We thank Professor Timothy J. Hall and his research group at the University of Wisconsin-Madision for providing the phantom dataset.

This work was supported by the National Science Foundation under Grant Nos. 1148111 and 1148124; and the National Institutes of Health under Grant No. NCI-R01CA140271.

Sandia National Laboratories is a multimission laboratory managed and operated by National Technology and Engineering Solutions of Sandia, LLC., a wholly owned subsidiary of Honeywell International, Inc., for the U.S. Department of Energy's National Nuclear Security Administration under contract DE-NA-0003525. This paper describes objective technical results and analysis. Any subjective views or opinions that might be expressed in the paper do not necessarily represent the views of the U.S. Department of Energy or the United States Government.

This paper describes objective technical results and analysis. Any subjective views or opinions that might be expressed in the paper do not necessarily represent the views of the U.S. Department of Energy or the United States Government.

References

References

[1] P. Barbone, A. Oberai, A review of the mathematical and computational foundations of biomechanical imaging, in: Computational Modeling in Biomechanics, Springer, 2010, pp. 375–408.

[2] M. S. Richards, P. E. Barbone, A. A. Oberai, Quantitative three-dimensional elasticity imaging from quasi-static deformation: a phantom study, Physics in medicine and biology 54 (3) (2009) 757.

[3] O. A. Babaniyi, A. A. Oberai, P. E. Barbone, Recovering vector displacement estimates in quasistatic elastography using sparse relaxation of the momentum equation, Inverse Problems in Science and Engineering 25 (3) (2017) 326–362. doi:10.1080/17415977.2016.1161034.
URL http://www.tandfonline.com/doi/ref/10.1080/17415977.2016.1161034

[4] P. E. Barbone, N. H. Gokhale, Elastic modulus imaging: on the uniqueness and nonuniqueness of the elastography inverse problem in two dimensions, Inverse Problems 20 (1) (2004) 283. doi:10.1088/0266-5611/20/1/017.
URL http://stacks.iop.org/0266-5611/20/i=1/a=017

[5] P. E. Barbone, A. A. Oberai, Elastic modulus imaging: some exact solutions of the compressible elastography inverse problem, Physics in Medicine and Biology 52 (6) (2007) 1577. doi:10.1088/0031-9155/52/6/003.
URL http://stacks.iop.org/0031-9155/52/i=6/a=003

[6] U. Albocher, P. E. Barbone, A. A. Oberai, I. Harari, Uniqueness of inverse problems of isotropic incompressible three-dimensional elasticity, Journal of the Mechanics and Physics of Solids 73 (2014) 55–68. doi:10.1016/j.jmps.2014.08.010.
URL http://www.sciencedirect.com/science/article/pii/S002250961400177X

[7] U. Albocher, A. A. Oberai, P. E. Barbone, I. Harari, Adjoint-weighted equation for inverse problems of incompressible plane-stress elasticity, Computer Methods in Applied Mechanics and Engineering 198 (30–32) (2009) 2412–2420. doi:10.1016/j.cma.2009.02.034.
URL http://www.sciencedirect.com/science/article/pii/S004578250900111X

[8] P. E. Barbone, C. E. Rivas, I. Harari, U. Albocher, A. A. Oberai, Y. Zhang, Adjoint-weighted variational formulation for the direct solution of inverse problems of general linear elasticity with full interior data, International Journal for Numerical Methods in Engineering 81 (13) (2010) 1713–1736. doi:10.1002/nme.2760.
URL http://onlinelibrary.wiley.com/doi/10.1002/nme.2760/abstract

[9] E. Ozkan, O. Goksel, Compliance boundary conditions for patient-specific deformation simulation using the finite element method, Biomedical Physics & Engineering Express 4 (2) (2018) 025003.

[10] D. T. Seidl, A computational framework for elliptic inverse problems with uncertain boundary conditions, Ph.D. thesis, Boston University (2015).

[11] D. T. Seidl, B. G. van Bloemen Waanders, T. M. Wildey, Simultaneous inversion of shear modulus and traction boundary conditions in biomechanical imaging, Inverse Problems in Science and Engineering (2019) 1–21.

[12] M. I. Diaz, W. Aquino, M. Bonnet, A modified error in constitutive equation approach for frequency-domain viscoelasticity imaging using interior data, Computer methods in applied mechanics and engineering 296 (2015) 129–149.

[13] S. Ghosh, Z. Zou, O. Babaniyi, W. Aquino, M. I. Diaz, M. Bayat, M. Fatemi, Modified error in constitutive equations (mece) approach for ultrasound elastography, The Journal of the Acoustical Society of America 142 (4) (2017) 2084–2093.

[14] W. Aquino, M. Bonnet, Analysis of the error in constitutive equation approach for time-harmonic elasticity imaging, SIAM Journal on Applied Mathematics 79 (3) (2019) 822–849.

[15] R. F. Stengel, Optimal control and estimation, Courier Corporation, 1994.

[16] M. Asch, M. Bocquet, M. Nodet, Data assimilation: methods, algorithms, and applications, Vol. 11, SIAM, 2016.

[17] D. González, A. Badías, I. Alfaro, F. Chinesta, E. Cueto, Model order reduction for real-time data assimilation through extended kalman filters, Computer Methods in Applied Mechanics and Engineering 326 (2017) 679–693.

[18] D. Simon, Kalman filtering with state constraints: a survey of linear and nonlinear algorithms, IET Control Theory & Applications 4 (8) (2010) 1303–1318.

[19] V. Girault, G. V. Pencheva, M. F. Wheeler, T. M. Wildey, Domain decomposition for linear elasticity with dg jumps and mortars, Computer Methods in Applied Mechanics and Engineering 198 (21-26) (2009) 1751–1765.

[20] J. H. Wang, J.-S. Lin, Cell traction force and measurement methods, Biomechanics and modeling in mechanobiology 6 (6) (2007) 361–371.

[21] R. W. Style, R. Boltyanskiy, G. K. German, C. Hyland, C. W. MacMinn, A. F. Mertz, L. A. Wilen, Y. Xu, E. R. Dufresne, Traction force microscopy in physics and biology, Soft matter 10 (23) (2014) 4047–4055.

[22] A. Tarantola, Inverse Problem Theory: Methods for Data Fitting and Model Parameter Estimation, Elsevier Science, 2002.

[23] R. H. Byrd, P. Lu, J. Nocedal, C. Zhu, A limited memory algorithm for bound constrained optimization, SIAM Journal on Scientific and Statistical Computing 16 (5) (1995) 1190–1208.

[24] T. Z. Pavan, E. L. Madsen, G. R. Frank, J. Jiang, A. A. Carneiro, T. J. Hall, A nonlinear elasticity phantom containing spherical inclusions, Physics in Medicine and Biology 57 (15) (2012) 4787.

[25] J. Francois Dord, S. Goenezen, A. A. Oberai, P. E. Barbone, J. Jiang, T. J. Hall, T. Pavan, Validation of quantitative linear and nonlinear compression elastography, Ultrasound Elastography for Biomedical Applications and Medicine (2018) 129–142.

[26] J. Jiang, T. J. Hall, A fast hybrid algorithm combining regularized motion tracking and predictive search for reducing the occurrence of large displacement errors, IEEE Transactions on Ultrasonics, Ferroelectrics, and Frequency Control 58 (4) (2011) 730–736.

[27] B. Banerjee, T. F. Walsh, W. Aquino, M. Bonnet, Large scale parameter estimation problems in frequency-domain elastodynamics using an error in constitutive equation functional, Computer methods in applied mechanics and engineering 253 (2013) 60–72.

[28] J. E. Warner, M. I. Diaz, W. Aquino, M. Bonnet, Inverse material identification in coupled acoustic-structure interaction using a modified error in constitutive equation functional, Computational mechanics 54 (3) (2014) 645–659.

[29] M. Bonnet, W. Aquino, Three-dimensional transient elastodynamic inversion using the modified error in constitutive relation, Journal of Physics: Conference Series 542 (2014) 012003. doi:10.1088/1742-6596/542/1/012003.
URL https://doi.org/10.1088%2F1742-6596%2F542%2F1%2F012003

Appendix A. Natural BC

In this appendix we derive the natural BC implied by the last term in the equation (9). Throughout this section we use the "comma" derivative notation $u_{,i} := \frac{\partial u}{\partial x_i}$.

Using the Euler-Lagrange equation (12) in (9) yields the weak boundary condition:

$$\langle \delta \boldsymbol{u}, \mu \boldsymbol{A}(\boldsymbol{w}) \cdot \boldsymbol{n} \rangle - \langle \boldsymbol{w}, \mu \boldsymbol{A}(\delta \boldsymbol{u}) \cdot \boldsymbol{n} \rangle = 0 \ \forall \delta \boldsymbol{u} \in \mathcal{V} \tag{A.1}$$

We now introduce a scalar field $\phi(\boldsymbol{x})$ that is equal to a constant C for all $\boldsymbol{x} \in \Gamma$ and is greater than C for all $\boldsymbol{x} \in \Omega$. We then define $\delta \boldsymbol{u}$ as:

$$\delta \boldsymbol{u} := \phi \boldsymbol{w}. \tag{A.2}$$

Substituting (A.2) into (A.1) yields

$$\int_\Gamma \phi w_i (\mu A_{ij}(\boldsymbol{w}) n_j) \ d\Gamma - \int_\Gamma w_i (\mu A_{ij}(\phi \boldsymbol{w}) n_j) \ d\Gamma = 0 \ \forall \ \phi \boldsymbol{w} \in \mathcal{V}. \tag{A.3}$$

Note that the definition of ϕ implies that

$$\nabla \phi(\boldsymbol{x}) | \boldsymbol{x} \in \Gamma = -\|\nabla \phi\| \boldsymbol{n}. \tag{A.4}$$

Therefore $A_{ij}(\phi \boldsymbol{w}) n_j$ for $\boldsymbol{x} \in \Gamma$ may be computed to be:

$$\begin{aligned} A_{ij}(\phi \boldsymbol{w}) n_j &= \big[2\phi_{,k} w_k \delta_{ij} + \phi_{,i} w_j + \phi_{,j} w_i\big] n_j + \big[2\phi w_{k,k} \delta_{ij} + \phi w_{j,i} + \phi w_{i,j}\big] n_j, \\ &= -\|\nabla \phi(\boldsymbol{x})\| \big[2 n_k a_k \delta_{ij} + n_i a_j + n_j a_i\big] n_j + \phi A_{ij}(\boldsymbol{w}) n_j, \\ &= -3\|\nabla \phi(\boldsymbol{x})\| n_i a_n - \|\nabla \phi(\boldsymbol{x})\| a_i + \phi A_{ij}(\boldsymbol{w}) n_j, \\ &= -4\|\nabla \phi(\boldsymbol{x})\| n_i a_n - \|\nabla \phi(\boldsymbol{x})\| a_j \tau_{ij} + \phi A_{ij}(\boldsymbol{w}) n_j. \end{aligned} \tag{A.5}$$

In (A.5), we introduced $\tau_{ij} = \delta_{ij} - n_i n_j$, which gives the tangential component of any vector, and $a_n := a_i n_i$. Substituting (A.5) into (A.3) gives

$$\begin{aligned} -\int_\Gamma \mu w_i (-4\|\nabla \phi(\boldsymbol{x})\| n_i w_n - \|\nabla \phi(\boldsymbol{x})\| w_j \tau_{ij}) \ d\Gamma \\ = \int_\Gamma \mu \|\nabla \phi(\boldsymbol{x})\| \left(4 w_n w_n + w_\tau w_\tau\right) \ d\Gamma = 0 \ \forall \quad \phi \boldsymbol{w} \in \mathcal{V}. \end{aligned} \tag{A.6}$$

The integrand in (A.6) is clearly non-negative for any $\boldsymbol{w}$, so we conclude that $\boldsymbol{w}$ must vanish on the boundary.

Appendix B. General CASE Inverse Formulation

In this appendix we discuss a more general CASE-based inverse formulation that allows for the use of different weighting tensors in the data match terms for the CASE and inverse problem Lagrangians.

We utilize the following Lagrangian to define the CASE data assimilation PDEs, which will serve as the PDE constraint in the inverse problem:

$$\mathcal{L}^{\text{CASE}}(\boldsymbol{u},\boldsymbol{w}) = \frac{1}{2}\left(\boldsymbol{u}-\boldsymbol{u}^m, \boldsymbol{D}(\boldsymbol{u}-\boldsymbol{u}^m)\right) + a(\boldsymbol{w},\boldsymbol{u};\mu) - \frac{\tau}{2h}\left\langle \boldsymbol{w},\boldsymbol{w}\right\rangle, \tag{B.1}$$

where

$$a(\boldsymbol{w},\boldsymbol{u};\mu) := (\nabla \boldsymbol{w}, \mu \boldsymbol{A}(\boldsymbol{u})) - \left\langle \boldsymbol{w}, \mu \boldsymbol{A}(\boldsymbol{u})\cdot \boldsymbol{n}\right\rangle. \tag{B.2}$$

For this problem we classify $\boldsymbol{u}$ and $\boldsymbol{w}$ as state variables and use Greek letters $\boldsymbol{\gamma}$ and $\boldsymbol{\lambda}$ for the adjoint variables. The relevant function spaces are

$$\boldsymbol{u},\boldsymbol{\gamma},\in \mathcal{S} := \{\boldsymbol{v} \mid v_i \in H^1(\Omega)\}, \tag{B.3}$$

$$\boldsymbol{w},\boldsymbol{\lambda} \in \mathcal{V} := \{\boldsymbol{v} \mid v_i \in H^1(\Omega)\}. \tag{B.4}$$

As in section 3, the strongly-stabilized CASE variant can be obtained by setting $\mathcal{V} = \mathcal{V}_0 := \{\boldsymbol{v} \mid v_i \in H^1(\Omega), v_i = 0 \text{ on } \Gamma\}$.

We take variations of (B.1) to obtain the following weak forms:

$$D_{\boldsymbol{u}}\mathcal{L}^{\text{CASE}}\cdot\boldsymbol{\gamma} = (\boldsymbol{\gamma}, \boldsymbol{D}(\boldsymbol{u}-\boldsymbol{u}^m))_\Omega + a(\boldsymbol{w},\boldsymbol{\gamma};\mu) \overset{set}{=} 0 \ \forall \boldsymbol{\gamma}\in\mathcal{S} \tag{B.5}$$

$$D_{\boldsymbol{w}}\mathcal{L}^{\text{CASE}}\cdot\boldsymbol{\lambda} = a(\boldsymbol{\lambda},\boldsymbol{u};\mu) - \frac{\tau}{h}(\boldsymbol{\lambda},\boldsymbol{w})_\Gamma \overset{set}{=} 0 \ \forall \boldsymbol{\lambda}\in\mathcal{V} \tag{B.6}$$

Equations (B.5) and (B.6) motivate the introduction of the following tetralinear form:

$$b(\boldsymbol{\gamma},\boldsymbol{\lambda},\boldsymbol{u},\boldsymbol{w};\mu) \equiv (\boldsymbol{\gamma}, \boldsymbol{D}(\boldsymbol{u}-\boldsymbol{u}^m))_\Omega + a(\boldsymbol{w},\boldsymbol{\gamma};\mu) + a(\boldsymbol{\lambda},\boldsymbol{u};\mu) - \frac{1}{h}(\boldsymbol{\lambda},\boldsymbol{w})_\Gamma \tag{B.7}$$

The Lagrangian that defines the PDE-constrained optimization problem, $\mathcal{L}^{\text{OPT}}$, can use a data match term that is completely different from the one presented in $\mathcal{L}^{\text{CASE}}$. For demonstration purposes we choose a least squares term with an arbitrary weighting tensor $\boldsymbol{W}$. We also include a regularization term $\mathcal{R}(\mu)$ and constant α that determines its strength. The Lagrangian is

$$\mathcal{L}^{\text{OPT}}(\boldsymbol{\gamma},\boldsymbol{\lambda},\boldsymbol{u},\boldsymbol{w},\mu) = \frac{1}{2}\left(\boldsymbol{u}-\boldsymbol{u}^m, \boldsymbol{W}(\boldsymbol{u}-\boldsymbol{u}^m)\right) + \alpha\mathcal{R}(\mu) + b(\boldsymbol{\gamma},\boldsymbol{\lambda},\boldsymbol{u},\boldsymbol{w};\mu). \tag{B.8}$$

The forward problem is derived by taking variations of (B.8) w.r.t the adjoint variables:

$$D_{\boldsymbol{\gamma}}\mathcal{L}^{\mathrm{OPT}}\cdot\delta\boldsymbol{\gamma}+D_{\boldsymbol{\lambda}}\mathcal{L}^{\mathrm{OPT}}\cdot\delta\boldsymbol{\lambda}=b(\delta\boldsymbol{\gamma},\delta\boldsymbol{\lambda},\boldsymbol{u},\boldsymbol{w};\mu)\stackrel{set}{=}0\ \forall(\delta\boldsymbol{\gamma},\delta\boldsymbol{\lambda})\in\mathcal{S}\times\mathcal{V}. \quad \text{(B.9)}$$

The discrete form of the forward problem (borrowing notation from the previous section) is

$$\begin{bmatrix}[M_D] & [K]^T\\ [K] & -[S]\end{bmatrix}\begin{Bmatrix}u\\ w\end{Bmatrix}=\begin{Bmatrix}[M_D]u^m\\ \mathbf{0}\end{Bmatrix}. \quad \text{(B.10)}$$

The adjoint problem is obtained by taking variations of (B.8) w.r.t. the state equation variables:

$$\begin{aligned}D_{\boldsymbol{u}}\mathcal{L}^{\mathrm{OPT}}\cdot\delta\boldsymbol{u}&=(\delta\boldsymbol{u},\boldsymbol{W}(\boldsymbol{u}-\boldsymbol{u}^m))_\Omega+(\boldsymbol{\gamma},\boldsymbol{D}\delta\boldsymbol{u})_\Omega+a(\boldsymbol{\lambda},\delta\boldsymbol{u};\mu) \quad \text{(B.11)}\\ &\stackrel{set}{=}0\ \forall\delta\boldsymbol{u}\in\mathcal{S},\\ D_{\boldsymbol{w}}\mathcal{L}^{\mathrm{OPT}}\cdot\delta\boldsymbol{w}&=a(\delta\boldsymbol{w},\boldsymbol{\gamma};\mu)-\frac{1}{h}(\delta\boldsymbol{w},\boldsymbol{\gamma})_\Gamma\stackrel{set}{=}0\ \forall\delta\boldsymbol{w}\in\mathcal{V}. \quad \text{(B.12)}\end{aligned}$$

Next we discretize (B.11) and (B.12) and observe that the block matrix in the discrete adjoint system (B.13) is the transpose of the one in (B.10). These matrices are, however, identical because $[M_D]$ and $[S]$ are symmetric. Thus the forward and adjoint systems differ only in their right hand sides.

$$\begin{bmatrix}[M_D] & [K]^T\\ [K] & -[S]\end{bmatrix}\begin{Bmatrix}\gamma\\ \lambda\end{Bmatrix}=\begin{Bmatrix}-[M_W](u-u^m)\\ \mathbf{0}\end{Bmatrix} \quad \text{(B.13)}$$

To determine the gradient we examine the total differential of $\mathcal{L}^{\mathrm{OPT}}$ and note that after solving (B.10) and (B.13) only the μ variation is non-zero.

$$\begin{aligned}\delta\mathcal{L}^{\mathrm{OPT}}&=\cancel{D_{\boldsymbol{\gamma}}\mathcal{L}^{\mathrm{OPT}}\cdot\delta\boldsymbol{\gamma}}+\cancel{D_{\boldsymbol{\lambda}}\mathcal{L}^{\mathrm{OPT}}\cdot\delta\boldsymbol{\lambda}} \quad \text{(B.14)}\\ &+\cancel{D_{\boldsymbol{u}}\mathcal{L}^{\mathrm{OPT}}\cdot\delta\boldsymbol{u}}+\cancel{D_{\boldsymbol{w}}\mathcal{L}^{\mathrm{OPT}}\cdot\delta\boldsymbol{w}}+D_\mu\mathcal{L}^{\mathrm{OPT}}\cdot\delta\mu\\ D_\mu\mathcal{L}^{\mathrm{OPT}}\cdot\delta\mu&=a(\boldsymbol{w},\boldsymbol{\gamma},\delta\mu)+a(\boldsymbol{\lambda},\boldsymbol{u},\delta\mu)+\alpha D_\mu\mathcal{R}\cdot\delta\mu \quad \text{(B.15)}\end{aligned}$$

We now present a simplification that occurs when $\boldsymbol{W} = \boldsymbol{D}$. Expanding (B.9) using (B.7) yields

$$(\delta\boldsymbol{\gamma}, \boldsymbol{D}(\boldsymbol{u} - \boldsymbol{u}^m))_\Omega + a(\boldsymbol{w}, \delta\boldsymbol{\gamma}; \mu) + a(\delta\boldsymbol{\lambda}, \boldsymbol{u}; \mu) - \frac{1}{h}(\delta\boldsymbol{\lambda}, \boldsymbol{w})_\Gamma = 0 \ \forall (\delta\boldsymbol{\gamma}, \delta\boldsymbol{\lambda}) \in \mathcal{S} \times \mathcal{V}. \tag{B.16}$$

We combine equations (B.11) and (B.12) to produce

$$(\boldsymbol{\gamma}, \boldsymbol{D}\delta\boldsymbol{u})_\Omega + a(\boldsymbol{\lambda}, \delta\boldsymbol{u}; \mu) + (\delta\boldsymbol{u}, \boldsymbol{W}(\boldsymbol{u} - \boldsymbol{u}^m))_\Omega + a(\delta\boldsymbol{w}, \gamma; \mu) - \frac{1}{h}(\delta\boldsymbol{w}, \boldsymbol{\lambda})_\Gamma = 0 \ \forall (\delta\boldsymbol{u}, \delta\boldsymbol{w}) \in \mathcal{S} \times \mathcal{V}. \tag{B.17}$$

The zero function is a member of $\mathcal{V}$. We make the substitutions $\boldsymbol{0} \leftarrow \delta\boldsymbol{\lambda}, \delta\boldsymbol{w}$ in (B.16) and (B.17), and $\delta\boldsymbol{u} \leftarrow \delta\boldsymbol{\gamma}$ in (B.16) to arrive at

$$(\delta\boldsymbol{u}, \boldsymbol{D}(\boldsymbol{u} - \boldsymbol{u}^m)_\Omega + a(\boldsymbol{w}, \delta\boldsymbol{u}; \mu) = 0 \ \forall \delta\boldsymbol{u} \in \mathcal{S}, \tag{B.18}$$

$$(\boldsymbol{\gamma}, \boldsymbol{D}\delta\boldsymbol{u}) + a(\boldsymbol{\lambda}, \delta\boldsymbol{u}; \mu) + (\delta\boldsymbol{u}, \boldsymbol{W}(\boldsymbol{u} - \boldsymbol{u}^m))_\Omega = 0 \ \forall \delta\boldsymbol{u} \in \mathcal{S}. \tag{B.19}$$

Now we choose $\boldsymbol{W} = \boldsymbol{D}$ and subtract (B.18) from (B.19) to obtain

$$(\boldsymbol{\gamma}, \boldsymbol{D}\delta\boldsymbol{u})_\Omega + a(\boldsymbol{\lambda} - \boldsymbol{w}, \delta\boldsymbol{u}; \mu) = 0 \ \forall \delta\boldsymbol{u} \in \mathcal{S}. \tag{B.20}$$

We find that (B.20) is satisfied identically by the fields $\boldsymbol{\gamma} = \boldsymbol{0}$ and $\boldsymbol{\lambda} = \boldsymbol{w}$. Application of these results to equation (B.15) yields the following simplified expression for the gradient:

$$D_\mu \mathcal{L}^{\mathrm{OPT}} \cdot \delta\mu = \cancel{a(\boldsymbol{w}, \boldsymbol{\gamma}; \delta\mu)} + a(\boldsymbol{w}, \boldsymbol{u}; \delta\mu) + \alpha D_\mu \mathcal{R} \cdot \delta\mu. \tag{B.21}$$

Thus if we use the same data match terms in $\mathcal{L}^{\mathrm{CASE}}$ and $\mathcal{L}^{\mathrm{OPT}}$ the solution of a single linear system (B.10) is necessary to obtain the fields used to compute the value of the objective function and its gradient, consistent with the formulation presented in section 3. Otherwise we must solve two block linear systems with different right hand sides.

Appendix C. Phantom Displacement Fields

This appendix contains the measured and predicted displacement fields from the phantom datasets, excluding those from Target 1 that are contained in section 4. We also present the lateral displacement fields obtained from the strongly-stabilized CASE formulation for comparison purposes.

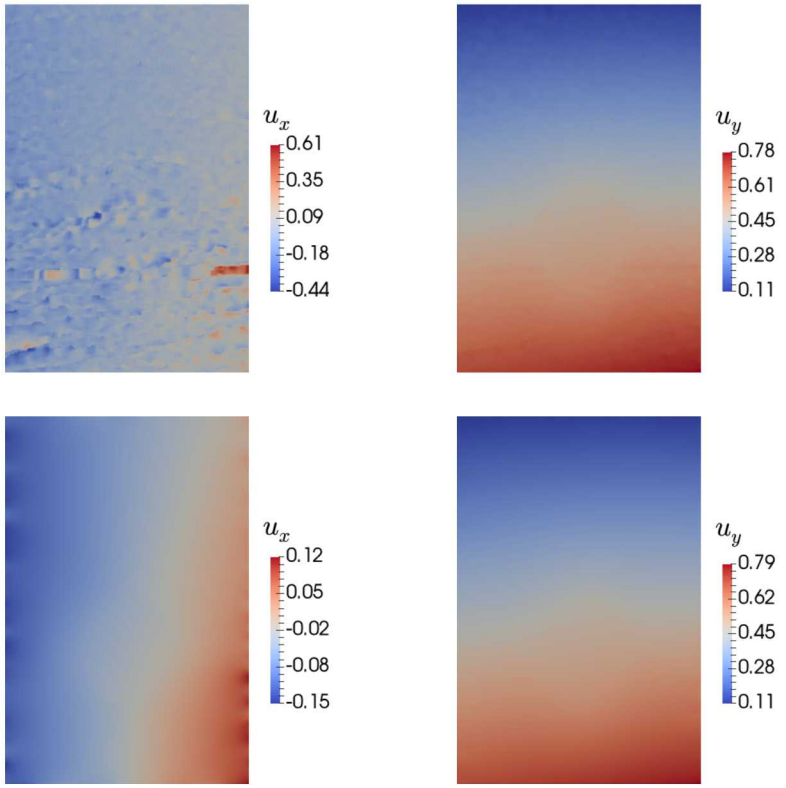

Figure C.10: The measured (top row) and predicted (bottom row) displacement fields (in mm) obtained from the weakly-stabilized formulation for Target 2.

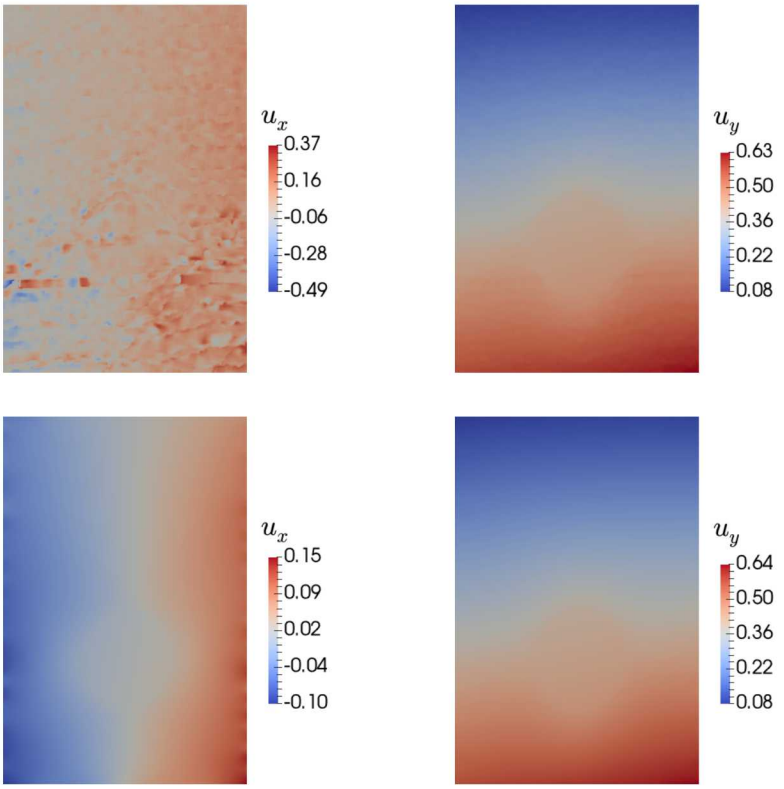

Figure C.11: The measured (top row) and predicted (bottom row) displacement fields (in mm) obtained from the weakly-stabilized formulation for Target 3.

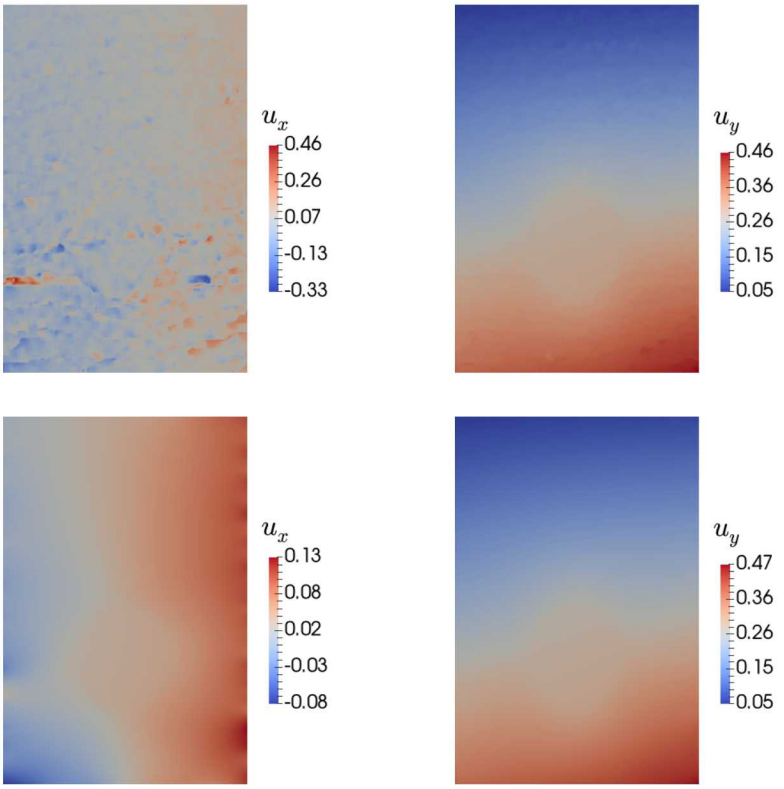

Figure C.12: The measured (top row) and predicted (bottom row) displacement fields (in mm) obtained from the weakly-stabilized formulation for Target 4.

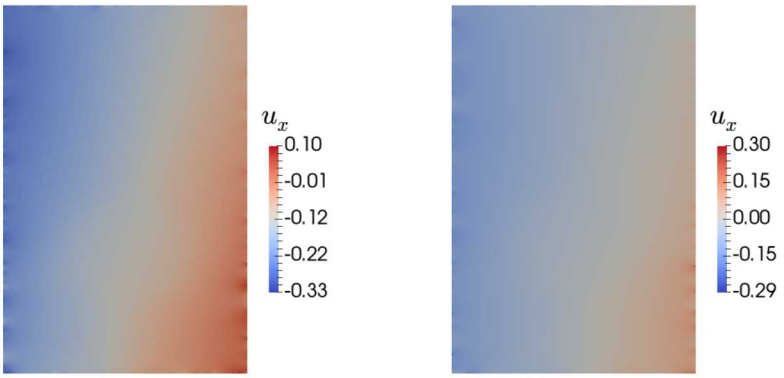

Target 1 Target 2

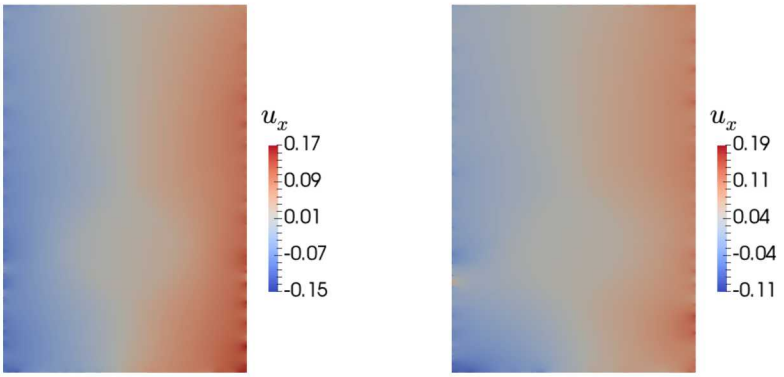

Target 3 Target 4

Figure C.13: The predicted lateral displacement fields (in mm) for all targets from the strongly-stabilized formulation. The fluctuations on the boundary are larger and higher in frequency than those observed in the weakly-stabilized results.